

ANALYSIS AND USAGE OF THE QUIKSCAT CALIBRATION  
GROUND STATION

by

Arden Anderson

A thesis submitted to the faculty of

Brigham Young University

in partial fulfillment of the requirements for the degree of

Master of Science

Department of Electrical and Computer Engineering

Brigham Young University

August 2001



Copyright © 2001 Arden Anderson

All Rights Reserved



BRIGHAM YOUNG UNIVERSITY

GRADUATE COMMITTEE APPROVAL

of a thesis submitted by

Arden Anderson

This thesis has been read by each member of the following graduate committee and by majority vote has been found to be satisfactory.

\_\_\_\_\_

Date

\_\_\_\_\_

Dr. David G. Long, Chair

\_\_\_\_\_

Date

\_\_\_\_\_

Dr. Randal W. Beard

\_\_\_\_\_

Date

\_\_\_\_\_

Dr. Kevin B. Smith



BRIGHAM YOUNG UNIVERSITY

As chair of the candidate's graduate committee, I have read the thesis of Arden Anderson in its final form and have found that (1) its format, citations, and bibliographical style are consistent and acceptable and fulfill university and department style requirements; (2) its illustrative materials including figures, tables, and charts are in place; and (3) the final manuscript is satisfactory to the graduate committee and is ready for submission to the university library.

---

Date

---

Dr. David G. Long  
Chair, Graduate Committee

Accepted for the Department

---

Dr. A. Lee Swindlehurst  
Graduate Coordinator

Accepted for the College

---

Dr. Douglas M. Chabries  
Dean, College of Engineering and Technology



## ABSTRACT

# ANALYSIS AND USAGE OF THE QUIKSCAT CALIBRATION GROUND STATION

Arden Anderson

Department of Electrical and Computer Engineering

Master of Science

Scatterometers are spaceborne microwave instruments operating in the C- or Ku-band. They measure the reflective properties of the Earth surface as they orbit the Earth. Scatterometer data is primarily used to determine the wind speed and direction over the Earth's ocean surface. The latest scatterometer mission is SeaWinds on QuikSCAT, launched by NASA Jet Propulsion Laboratory (JPL) in June of 1999. In order to insure the accuracy of the SeaWinds scatterometer, JPL has built a Calibration Ground Station (CGS) in White Sands, New Mexico. The CGS receives the signal of the SeaWinds instrument as the satellite passes overhead. Perturbations in the satellite's position, attitude and timing cause changes in the received signal. Comparing the actual received signal to a calculated, expected signal and resolving the differences in terms of position, attitude and timing perturbations is the strategy for validating SeaWinds operation using the CGS.

A geometry analysis provides a method to determine important parameters such as Doppler frequency and antenna pattern angles from the SeaWinds telemetry data. These become the basis for subsequent analyses with the CGS. A sensitivity analysis evaluates how the CGS data changes as a result of position, attitude and timing perturbations within their expected ranges for SeaWinds on QuikSCAT. A multipath analysis determines the multipath interference caused by the SeaWinds signal bouncing off the CGS surroundings. The analysis finds the multipath interference to be better than 60 dB below the desired signal and therefore small enough to neglect in CGS data processing. A frequency analysis presents a method to determine the center frequency of the transmitted SeaWinds pulses. This method is enhanced by a matched filter implementation, which is also used to reconstruct the SeaWinds antenna pattern.

## ACKNOWLEDGMENTS

My parents have always been a source of support. I herewith thank them for their love and encouragement. While I'm at it, I would like to thank my wife for her silent support of this work. For all the hours she let me put into this thesis. Never once did she complain. Not a single time did she worry about being home with the kids while I was compiling or documenting the research that went into this thesis. And as soon as I figure out who she is, it is to her that this work will be dedicated.



# Contents

<b>Acknowledgments</b>	<b>xi</b>
<b>List of Figures</b>	<b>xvii</b>
<b>1 Introduction</b>	<b>1</b>
1.1 Motivation . . . . .	1
1.2 Contributions . . . . .	2
1.3 Outline . . . . .	3
<b>2 Background</b>	<b>5</b>
2.1 Scatterometry Basics . . . . .	5
2.2 SeaWinds on QuikSCAT . . . . .	7
2.3 The Calibration Ground Station . . . . .	11
<b>3 QuikSCAT Geometry Calculations</b>	<b>15</b>
3.1 Coordinate Frames . . . . .	17
3.2 Rotation Matrices . . . . .	19
3.3 Results . . . . .	22
<b>4 Sensitivity Analysis</b>	<b>31</b>
4.1 Analysis Method . . . . .	31
4.2 Initial Sensitivity Results . . . . .	34
4.3 Improved Presentation of Results . . . . .	37
4.4 Conclusion . . . . .	41
<b>5 Multipath Analysis</b>	<b>43</b>

5.1	Discretization of Scatterers . . . . .	45
5.2	Geometry Analysis . . . . .	47
5.3	Interference Evaluation . . . . .	49
5.4	Analysis Results and Conclusion . . . . .	53
<b>6</b>	<b>QuikSCAT CGS Frequency Analysis</b>	<b>55</b>
6.1	CGS Data . . . . .	55
6.2	Expected Frequency Variation . . . . .	57
6.3	Steps in the Frequency Analysis . . . . .	58
<b>7</b>	<b>Matched Filter Implementation</b>	<b>65</b>
7.1	Filter Bank . . . . .	67
7.2	Benefits of the Matched Filter . . . . .	70
7.3	Conclusion . . . . .	70
<b>8</b>	<b>Conclusion</b>	<b>73</b>
8.1	Summary of Contributions . . . . .	73
8.2	Future Research . . . . .	74
	<b>Bibliography</b>	<b>78</b>

## List of Figures

2.1	An illustration of the basic operation of a wind scatterometer . . . . .	6
2.2	Artist's depiction of SeaWinds on QuikSCAT . . . . .	8
2.3	Overview of SeaWinds geometry . . . . .	9
2.4	Simulated daily QuikSCAT coverage . . . . .	10
2.5	SeaWinds egg and slice geometry . . . . .	11
2.6	Visualization of the four beams captured during a SeaWinds pass . . . . .	12
2.7	Students on top of the CGS, in front of the radome cover which protects the CGS antenna . . . . .	13
2.8	Antenna and RF subsystem . . . . .	14
3.1	Vector definitions for the SeaWinds CGS geometry . . . . .	16
3.2	Attitude definition . . . . .	17
3.3	Inertial and local coordinate frames . . . . .	18
3.4	Geographic coordinate frame . . . . .	19
3.5	Spacecraft antenna pattern . . . . .	23
3.6	CGS antenna pattern . . . . .	23
3.7	Visual representation of a mid latitude pass . . . . .	24
3.8	Range and Doppler between satellite and CGS during a mid pass . . . . .	25
3.9	Doppler frequency during time of CGS capture . . . . .	26
3.10	Simulation of SeaWinds antenna gain over a sixty second capture . . . . .	27
3.11	CGS antenna gain over a sixty second simulated capture . . . . .	27
3.12	Simulated ten second capture of CGS data . . . . .	28
3.13	Simulated data during ten second capture plotted against antenna azimuth and elevation angles . . . . .	29
3.14	Simulated data from Figure 3.13 plotted atop the antenna pattern . . . . .	30

4.1	Visual depiction of position errors along <b>S</b> , <b>T</b> , and <b>U</b> axes . . . . .	33
4.2	Gain and gain difference for position errors along the <b>T</b> axis for a mid pass . . . . .	34
4.3	Demonstration of sampling ambiguity . . . . .	35
4.4	Angle difference for position errors along the <b>U</b> axis for a mid pass . . . . .	36
4.5	Angle offsets for outer beam, 0.1° roll error . . . . .	37
4.6	Concise sensitivity results for outer beam, 0.1° roll . . . . .	38
4.7	Summary of sensitivity analysis results for roll, pitch, yaw and antenna azimuth . . . . .	39
4.8	Summary of sensitivity analysis results for shifts along <b>S</b> , <b>T</b> , and <b>U</b> and for a timing shift . . . . .	40
5.1	Visualization of multipath . . . . .	44
5.2	CGS site map . . . . .	45
5.3	Electronic map of area surrounding the ground station . . . . .	46
5.4	Surrounding terrain divided into 464 individual patches . . . . .	46
5.5	Geometry of an arbitrary surface patch . . . . .	47
5.6	Geometry results for surrounding buildings . . . . .	48
5.7	Geometry results for surrounding terrain . . . . .	49
5.8	Perpendicular slices through the CGS antenna pattern . . . . .	51
5.9	$\sigma^0$ dependence on incidence angle for scatterometers . . . . .	52
5.10	Interference-to-signal ratio as a function of azimuth angle of incoming signal . . . . .	53
5.11	Summation of interference-to-signal ratio . . . . .	54
6.1	QuikSCAT geometry including backward, side and forward looks . . . . .	56
6.2	Plot of Doppler effect and Doppler compensation . . . . .	57
6.3	20 ms window of CGS data . . . . .	59
6.4	Analysis of a typical received pulse . . . . .	60
6.5	Sample results of the initial frequency analysis . . . . .	61
6.6	Frequency enhancement techniques . . . . .	62
6.7	Resolution enhancement results for simulated data . . . . .	63

7.1	Frequency plan of the CGS . . . . .	66
7.2	Block diagram of matched filtering system . . . . .	67
7.3	Sample results from the filter bank . . . . .	68
7.4	Sample results from matched filter processing . . . . .	69
7.5	Reconstructed SeaWinds antenna pattern . . . . .	71



# Chapter 1

## Introduction

In June of 1997, the NASA Scatterometer NSCAT prematurely ceased operation due to a power failure on board the satellite. NSCAT had up to that point been observing the Earth for 9 months. The next planned scatterometer mission was SeaWinds, which was scheduled to launch aboard ADEOS II in March of 2001. Because of the early termination of NSCAT and the lack of scatterometer data, in August of 1997, NASA decided to build a second SeaWinds scatterometer out of spare parts from SeaWinds on ADEOS II and begin a new mission within 18 months. This scatterometer mission would be a rapid response mission and would take the name of QuikSCAT. QuikSCAT's purpose is to continue to take scatterometer data in NSCAT's place and to prepare all involved science teams for SeaWinds on ADEOS II.

As a part of QuikSCAT's calibration and validation, Jet Propulsion Laboratory (JPL) designed and built a Calibration Ground Station (CGS) in White Sands, New Mexico. The CGS receives the signal of the satellite as it passes overhead. In September of 1998, JPL contracted the Microwave Earth Remote Sensing (MERS) Laboratory at Brigham Young University (BYU) to analyze the operation of the CGS and use it to calibrate important parameters of the QuikSCAT satellite such as its position, attitude, frequency and timing.

### 1.1 Motivation

SeaWinds' primary purpose is to measure the wind speed and direction over the Earth's ocean surface. This wind data is used in applications such as weather

forecasting, storm detecting, ship routing, oil production and fishing and shrimp harvesting. Scatterometer data over land is also used in deforestation monitoring, vegetation classification and iceberg tracking [1]. One important factor in the success of SeaWinds is its high resolution, facilitated by the precision of the SeaWinds instrument.

In order to assure the accuracy and precision of the SeaWinds scatterometer, the instrument must be calibrated. There are several methods to accomplish this. One is to verify the end products of the wind retrieval, i.e. evaluate the wind measurements. Another method is to examine the transmitted signal of the instrument. Its correct operation can then be verified by comparing the received signal with the calculated expected signal. The pursuit of the second method is the reason for JPL's building the QuikSCAT CGS. This approach has the advantage of directly calibrating the scatterometer measurements, which is useful for future missions.

## 1.2 Contributions

In order to effectively use the CGS, it is necessary to create algorithms to calibrate the SeaWinds instrument parameters. It is also important to analyze the operation of the CGS and verify the feasibility of its use as a calibration tool. This thesis explores in detail some of the simulations and analyses run to accomplish this analysis and verification.

The first contribution this thesis provides is a simulation of the QuikSCAT satellite's geometry. Geometry data provides information such as the antenna pattern angles and Doppler shift that the transmitted signal undergoes. This in turn enables accurate modelling of the satellite signal as received by the ground station.

The second contribution is a perturbation sensitivity analysis of CGS data. Perturbations of satellite parameters such as timing and attitude cause the signal received by the CGS to change. Detecting these changes and comparing them with the original signal makes it possible to deduce the magnitude of the original perturbation. This type of analysis only works if the satellite perturbations cause a change in the CGS data large enough to detect. The sensitivity analysis determines the relationship

between the magnitude of the satellite perturbation and the change in amplitude of the signal received by the CGS.

This thesis also provides a multipath analysis of the ground station. The CGS antenna does not exist in isolation. Buildings and terrain surround it on all sides. Because of concerns about possible multipath interference, BYU students travelled to the CGS in White Sands, New Mexico and surveyed the surrounding area. With the collected survey data, the possible multipath effects were simulated. The multipath is found to be better than 60 dB lower than the desired signal. It is therefore small enough to neglect in further CGS data processing.

One major contribution of this thesis is a frequency analysis of the CGS data. The frequency analysis extracts the frequency from the received signal and compares it with the calculated expected frequency. The thesis explores different techniques to enhance the resolution of the frequency determination and also develops a matched filter by means of which it reduces the variance of the determined frequency to  $\pm 1$  kHz.

The final contribution of this thesis is its description of a matched filter to reconstruct the scatterometer's antenna pattern. Current knowledge of the antenna pattern stems from measurements taken before the satellite's launch. The measurements are precise, but limited to a  $10^\circ$  by  $10^\circ$  window in the main lobe antenna pattern. The antenna pattern reconstruction provides information on the antenna pattern over a more extensive range of angles. This information can be used to enhance subsequent CGS analyses of power, frequency and timing.

Since SeaWinds on QuikSCAT is a precursor to SeaWinds on ADEOS II, the Calibration techniques developed for the QuikSCAT mission can also be used for the ADEOS II mission. They can also be extended for use in subsequent satellite missions.

### **1.3 Outline**

This thesis is organized as follows. Chapter 2 begins with a treatment of basic scatterometry, describing scatterometer operation and data application. This is

followed by a description of the QuikSCAT mission with the details of its operation. The Calibration Ground Station is then introduced and described.

Chapter 3 illustrates the simulation of QuikSCAT's geometry and explains how the knowledge of its antenna pattern is exploited.

Chapter 4 introduces the sensitivity analysis. This describes the simulations run to determine how sensitive the signal received at the CGS is to perturbations in the attitude, position, timing and frequency of the satellite.

Chapter 5 explains the multipath analysis. It outlines how multipath interference was simulated for the CGS surroundings. It then presents the results and discusses how they affect the observed satellite signal.

Chapter 6 contains an explicit description of the frequency analysis. It explains the steps of extracting the frequency of the received signal. It also describes methods to use the frequency information to calibrate the satellite's timing and yaw. It discusses limitations of the frequency analysis and presents methods to overcome them.

Chapter 7 describes the matched filter implementation for the CGS data. It discusses how the CGS pulses are reconstructed in order to create the matched filter. It then evaluates the effect of the matched filter in lowering the noise of the CGS data. It also presents uses for the matched filter, such as power analysis enhancement or antenna pattern reconstruction.

Chapter 8 concludes the thesis with a summary of the results of this work, contributions and a discussion on future research.

## Chapter 2

### Background

As this thesis deals with the calibration of the QuikSCAT satellite and the SeaWinds scatterometer it carries aboard, this chapter provides an overview of scatterometry, including its principles and applications. It continues with an introduction to the QuikSCAT mission, laying out important details of the satellite and the SeaWinds instrument. The chapter concludes with a description of the Calibration Ground Station. It describes how the CGS receives the signal of the satellite and makes the data available for analysis.

#### 2.1 Scatterometry Basics

Ocean winds provide valuable information for the scientific community. As oceans occupy 70% of the earth's surface, much of the weather we experience on land originates over the oceans. Changes in near-ocean winds also cause changes in currents, which ultimately affect global ecology.

Knowledge of ocean winds has been limited to measurements made by ships and buoys. Such data is sparse and not always reliable. Spaceborne scatterometers overcome the limitations of traditional ocean wind retrieval. With extensive daily global coverage, scatterometers provide consistent, continual wind data and increase the number of ocean wind measurements by several orders of magnitude over those from ships and buoys.

A spaceborne scatterometer measures the microwave reflection properties of the Earth's surface. It accomplishes this by transmitting microwave pulses of energy toward the earth and measuring the strength of the signal reflected back toward the

satellite. The electrical characteristics of the earth's surface within the illuminated area dictate the amount of power reflected back. Smooth surfaces direct the bulk of the reflected energy away from the satellite, while rougher surfaces provide more scattering back in the direction from which the signal came. On the Earth's oceans, winds cause waves at different scales. Long range effects are manifest in large waves with wavelengths of several meters or more. Local winds result in small waves, also called capillary waves or cat's paws, which are modulated by the larger waves, as illustrated in Figure 2.1. Capillary waves have wavelengths within the centimeter range and are the main factor in reflecting power back to the satellite. Higher winds create more capillary waves, building a rougher surface and consequently reflecting more energy back to the satellite.

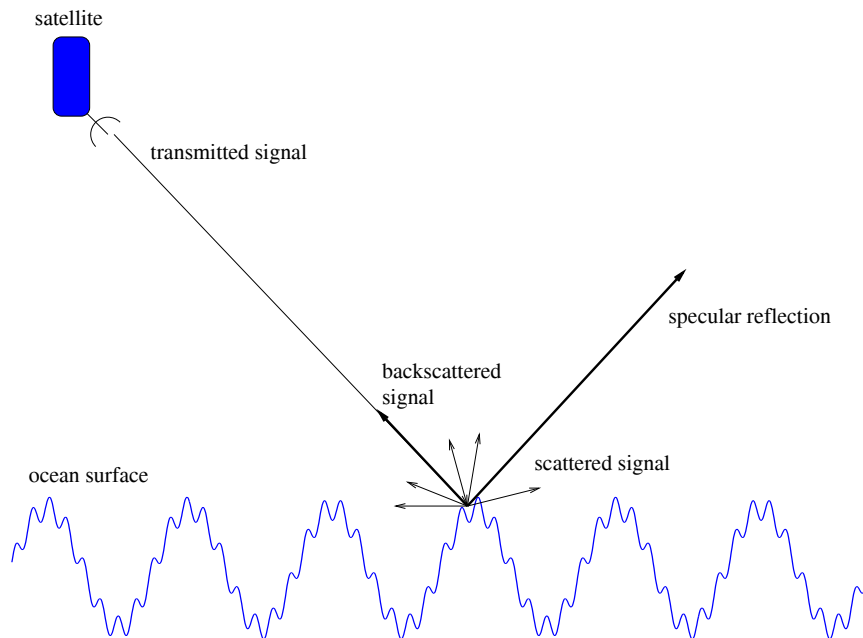


Figure 2.1: *An illustration of the basic operation of a wind scatterometer. Energy is transmitted down to the surface of the earth. This energy is partly absorbed, partly reflected. A large portion of the energy is reflected in the specular direction. The roughness of the surface determines how much is reflected back toward the satellite. The scatterometer measures this reflected energy.*

The reflective property of the surface, generally labelled as the normalized radar cross section, or  $\sigma^o$ , can be related to the received power,  $P_r$ , by a factor labelled “ $X$ ” [2], which is derived from the monostatic radar equation [3],

$$P_r = \frac{P_t G^2 \lambda^2 \sigma^o}{(4\pi)^3 R^4} = X \sigma^o, \quad (2.1)$$

where  $\lambda$  is the wavelength of the transmitted signal,  $R$  is the range of the satellite from the illuminated surface, and  $G$  is the antenna gain. The frequency of the transmitted signal is in the microwave spectrum, typically at Ku- or C-band. This range is used because of its ability to penetrate clouds and rain as the signal travels through the atmosphere. Wind speed and direction are related to  $\sigma^o$  by the geophysical model function. In order to retrieve the wind for a particular spot on the earth, several  $\sigma^o$  measurements at different azimuth angles are required. The scatterometer provides these measurements by illuminating each spot on the earth at different azimuth angles.

The first spaceborne scatterometer flew as a part of the Skylab missions in 1974. Since then the Seasat-A Satellite Scatterometer (SASS), the European Space Agency’s Remote Sensing Satellites (ERS-1 and ERS-2) and the NASA Scatterometer (NSCAT) have flown and successfully collected ocean wind data. The latest scatterometer mission is SeaWinds on QuikSCAT, which has been in operation since June of 1999.

## 2.2 SeaWinds on QuikSCAT

SeaWinds is the first of a new generation of scatterometers, first launched aboard the QuikSCAT satellite, shown in Figure 2.2, by NASA on June 19, 1999. The main difference between SeaWinds and its predecessors is its antenna. It uses a rotating pencil beam antenna as opposed to a fan beam antenna.

Fan beam scatterometers, such as NSCAT, deploy several fixed antennae to cast long, narrow footprints along the earth’s surface. The length of the footprint determines the width of the instrument’s swath. NSCAT cast beams down to both the left and right sides of the spacecraft, creating two parallel swaths with a gap in between, labelled the nadir gap. The narrow width of the footprint determines the

along track resolution. Cross track resolution is obtained by splitting the length of the footprint into bins by means of range or Doppler filtering. This technique results in  $7 \text{ km} \times 30 \text{ km}$  resolution of the data. One disadvantage is the physical bulkiness of the antennae on the spacecraft.



Figure 2.2: *Artist's depiction of SeaWinds on QuikSCAT.*

More compact satellites offer the advantage of lower launch costs and are therefore more desirable than bulkier designs. SeaWinds is designed with a rotating 1 m diameter dual beam parabolic dish antenna, making it lighter and more compact [4] than its predecessor, NSCAT. As shown in Figure 2.3, the parabolic dish focuses two beams at angles of  $40^\circ$  and  $46^\circ$  off of nadir (straight down) [5]. The beams are

labelled inner beam and outer beam, respectively. As the satellite moves along, the antenna spins at a constant rate of 18 revolutions per minute. This revolution creates a conical rotation of the beams which trace out a helical pattern on the surface of the earth, as pictured in Figure 2.4.

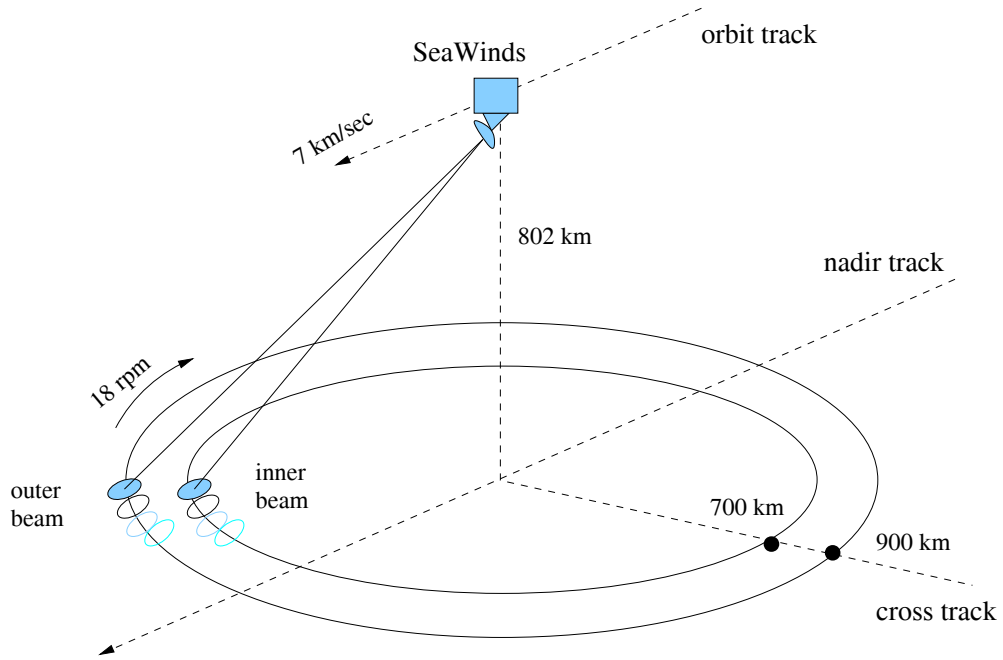


Figure 2.3: *Overview of SeaWinds geometry. QuikSCAT flies at an altitude of 802 km and a ground speed of 7 km/s. SeaWinds' rotating dish antenna rotates the inner and outer beams at 18 RPM to trace concentric circles with radii of 700 km and 900 km, respectively. Along track motion causes concentric circles to become concentric helices, as illustrated in Figure 2.4.*

The radii of the helices are 700 km and 900 km for the inner and outer beam, respectively. This results in two overlapping swaths with widths of 1400 km and 1800 km without a nadir gap, as seen in Figure 2.3. QuikSCAT flies at an altitude of 802 km in a near polar orbit, meaning its orbit is an ellipse, the track of which goes north to south and south to north, almost directly over the poles. The axial rotation of the earth causes the satellite's stationary orbit to effectively rotate around the earth,

allowing for complete coverage of the entire Earth's surface. QuikSCAT completes one full orbit in approximately 100 minutes. This translates into 14 orbits and more than 90% global coverage daily [5] (see Figure 2.4).

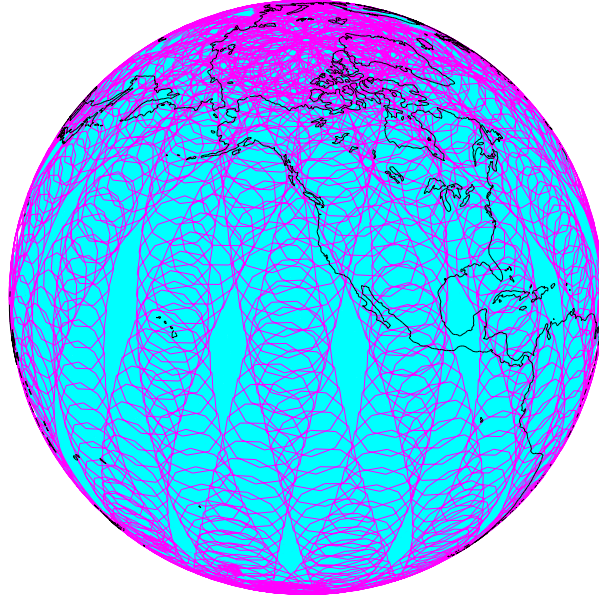


Figure 2.4: *Simulated daily QuikSCAT coverage. Sampling is decimated to clearly illustrate helical footprint trace. Areas not covered in one day show up as clear diamonds. These areas are covered in subsequent days. Poles receive extensive coverage.*

SeaWinds operates at a frequency of 13.402 GHz. It sends out a series of consecutive pulses, alternating beams (inner and outer) with each pulse. The pulses have a width, or duration, of 1.5 ms, with a pulse repetition interval (PRI) of 5.4 ms. Since the pulses alternate beams, the PRI for each beam is 10.8 ms. The footprints of the focused antenna beams have elliptical shapes. They are commonly called eggs and are of dimensions  $25 \text{ km} \times 35 \text{ km}$ . Further range filtering divides the eggs into slices, each approximately 5 km wide [6]. The resulting resolution for the slices is therefore  $5 \text{ km} \times 25 \text{ km}$ , as shown in Figure 2.5.

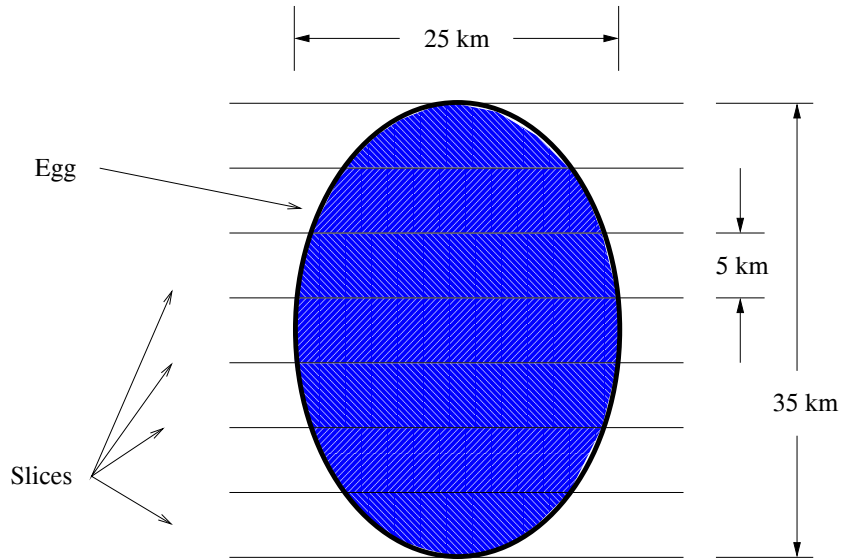


Figure 2.5: *SeaWinds egg and slice geometry. Nominal footprint (egg) dimensions are 25 km  $\times$  35 km. Range and Doppler filtering divide egg into 5 km  $\times$  25 km slices to improve resolution.*

### 2.3 The Calibration Ground Station

The accuracy of the SeaWinds scatterometer measurements is crucial for accurate wind measurement. For this reason, the task of calibrating the instrument is an important one. As part of the QuikSCAT calibration and validation efforts, JPL has built a Calibration Ground Station at the NASA White Sands Testing Facility in White Sands, New Mexico. Ground station platforms were used for NSCAT, ERS-1 and some SAR applications, but were implemented in a different fashion. Unlike the NSCAT calibration ground station, which both transmitted and received, the QuikSCAT calibration ground station (CGS) simply receives the signal of the satellite as it passes overhead.

QuikSCAT passes over the CGS approximately six times every eight days. During a typical pass, it illuminates the CGS four separate times. Initially, the CGS sees the outer beam as the satellite approaches, then the inner beam as it approaches. Next, after the satellite passes directly overhead, the CGS again sees the inner beam,

but as the satellite departs, or recedes away from the CGS. Finally, the CGS sees the outer beam as the satellite recedes, as shown in Figure 2.6.

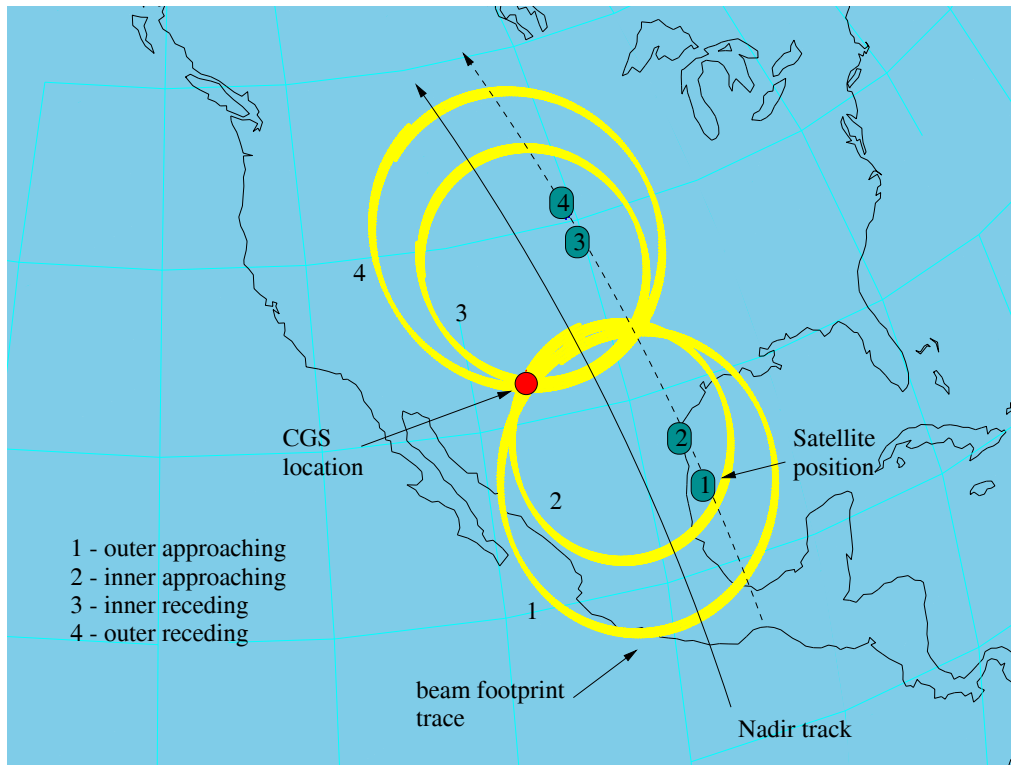


Figure 2.6: *Visualization of the four beams captured during a SeaWinds pass.*

Prior to illumination by SeaWinds, the CGS antenna is steered to point in the calculated direction of the spacecraft. Its position is then held constant as it receives 10 seconds worth of data from the satellite's signal. After the data capture, it is steered to point to the next calculated satellite position from which QuikSCAT's footprint will pass over the CGS [7].

If the angle at which QuikSCAT passes over the horizon is too small, the CGS only receives the outer beam as the QuikSCAT approaches and recedes. The CGS in this case captures the signal twice, for a period of 20 seconds each, instead of the conventional four captures of 10 seconds each.

The CGS employs a circularly polarized corrugated horn antenna, shown in Figure 2.8. The antenna has a 3 dB beamwidth of approximately  $20^\circ$ . The wide main beam minimizes sensitivity to CGS pointing errors. The antenna sits atop an azimuth/elevation mount which places it above the roof of the CGS. It is covered by a radome covering, as seen in Figure 2.7, to protect it from the elements.



Figure 2.7: *Students on top of the CGS, in front of the radome cover which protects the CGS antenna.*

The data received by the CGS is processed to determine any bias in position, attitude and timing of the QuikSCAT satellite. More details of the operation of SeaWinds on QuikSCAT and the Calibration Ground Station are given later.

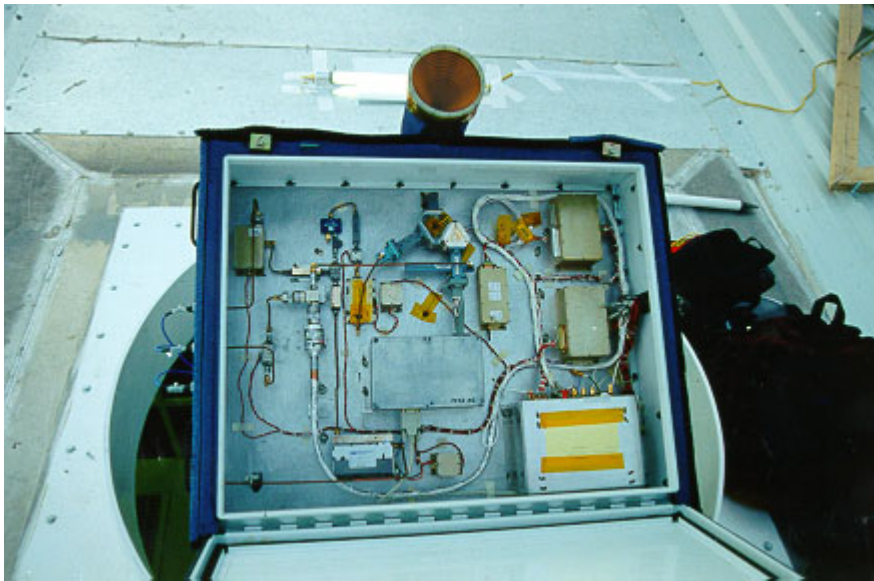
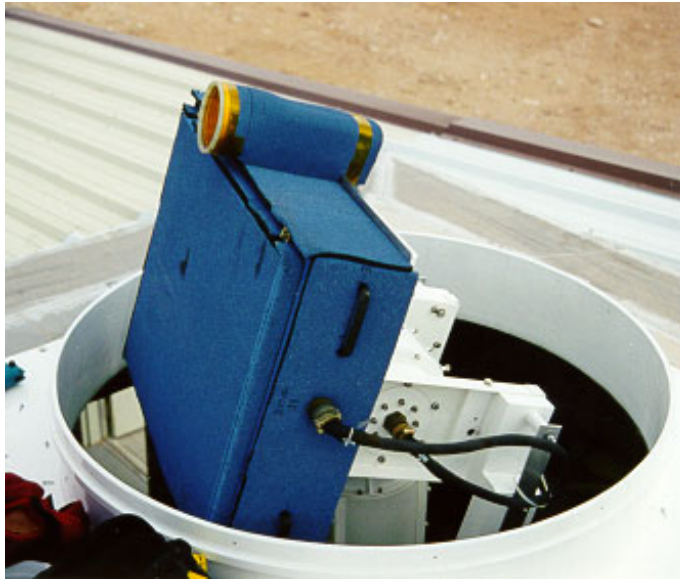


Figure 2.8: *Antenna and RF subsystem. Radome covering is removed and antenna pedestal is exposed. The top photograph shows the antenna from the side. The horn is the cylindrical unit on top. The bottom photograph shows the antenna from the front.*

## Chapter 3

### QuikSCAT Geometry Calculations

The basic strategy of the QuikSCAT CGS is to determine the expected transmitted power and frequency of the SeaWinds signal and compare it to the actual SeaWinds signal received by the ground station. Calculating the expected frequency requires knowledge of the Doppler effect upon the transmitted signal with respect to the CGS. Calculating the expected power of the received signal requires knowledge of the antenna gains of the receiving and transmitting antennas. The Doppler effect and the antenna gains require geometry calculations. Thus, calculating the QuikSCAT geometry is a fundamental task in the CGS data processing.

Basic SeaWinds telemetry data provides the inertial location vector ( $\mathbf{r}_s$ ), velocity vector ( $\mathbf{v}_s$ ) and attitude coordinates of the QuikSCAT satellite. The location and velocity vectors are defined in Figure 3.1. Attitude is given in terms of roll, pitch and yaw, defined in Figure 3.2. The Doppler effect of the received signal is obtained by calculating the relative velocity,  $v_{rel}$ , of the spacecraft with respect to the CGS by the equation

$$v_{rel} = \mathbf{v}_s \cdot (\mathbf{r}_g - \mathbf{r}_s), \quad (3.1)$$

where  $(\mathbf{r}_g - \mathbf{r}_s)$  is the vector connecting the spacecraft to the ground station and  $\mathbf{v}$  is the velocity vector, both in the inertial coordinate frame. The relative velocity is then applied, along with the wavelength,  $\lambda$ , of the signal to the equation

$$f_{dop} = \frac{v_{rel}}{\lambda}. \quad (3.2)$$

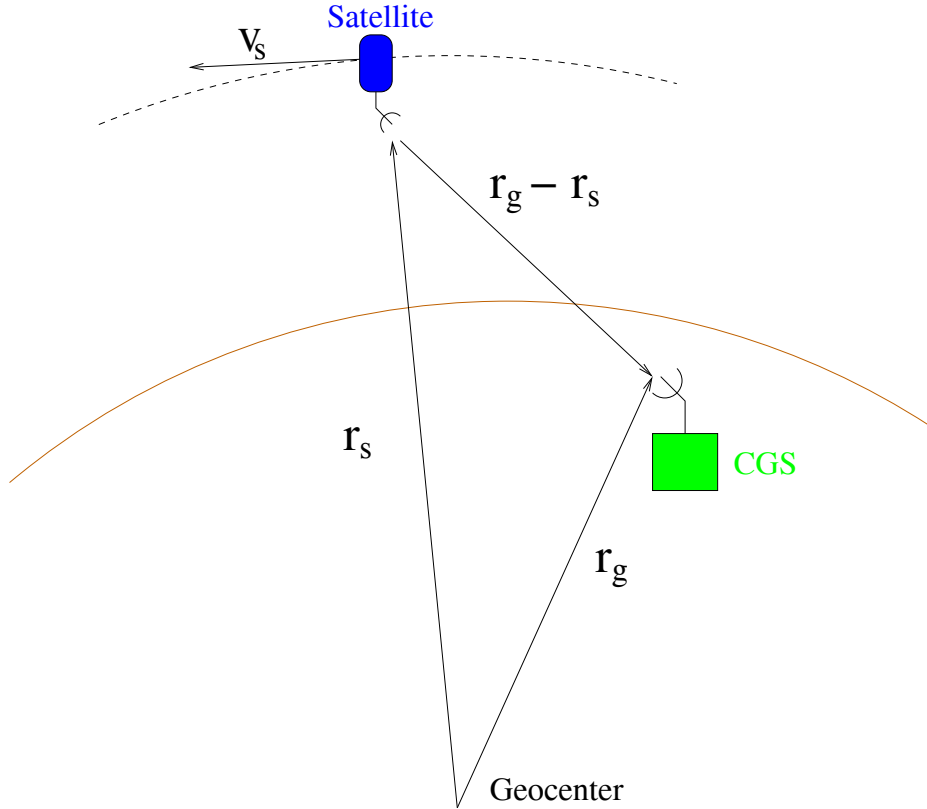


Figure 3.1: *Vector definitions for the SeaWinds CGS geometry.*

Traditionally, the Doppler frequency is calculated by dividing twice the relative velocity by the wavelength, which results in the two-way Doppler frequency. In this particular case, however, the signal received at the ground station is only affected by the one-way Doppler frequency, as defined in Eq. (3.2).

Calculating the power of the received signal requires knowledge of the antenna gains, which are calculated by converting the position and attitude of the spacecraft to antenna pattern vectors. This is accomplished through a series of rotation matrices. The remainder of this chapter familiarizes the reader with the QuikSCAT CGS geometry through an explanation of coordinate frames, followed by a detailed definition of each rotation matrix. The chapter concludes with sample results of the geometry calculations and an explanation of the types of trends expected in the power of the received signal.

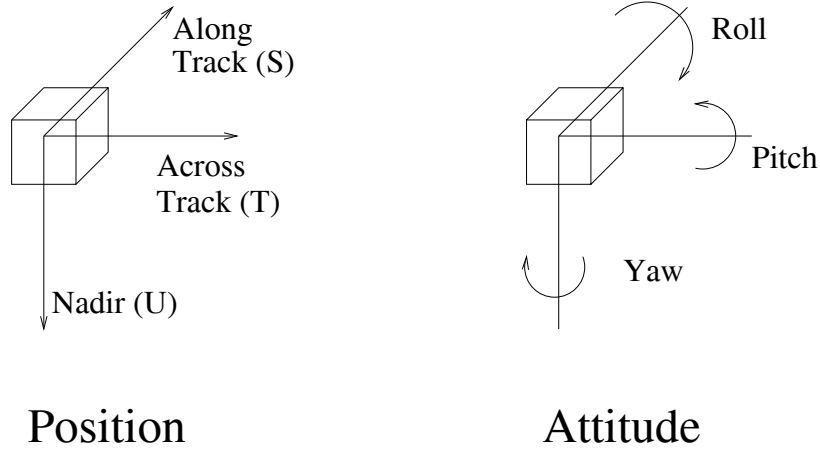


Figure 3.2: *Attitude definition.* The attitude coordinates, roll, pith and yaw, are defined by rotations about the spacecraft body coordinates,  $\mathbf{S}$ ,  $\mathbf{T}$ , and  $\mathbf{U}$ .

### 3.1 Coordinate Frames

The CGS geometry can be represented by the following seven coordinate frames,  $\mathcal{F}_I$ ,  $\mathcal{F}_g$ ,  $\mathcal{F}_{gA}$ ,  $\mathcal{F}_{gc}$ ,  $\mathcal{F}_{gd}$ ,  $\mathcal{F}_b$ , and  $\mathcal{F}_{sA}$ . These are defined below.

$\mathcal{F}_I$  is the inertial coordinate frame located at the center of the earth, with orthonormal basis vectors  $\{\mathbf{X}, \mathbf{Y}, \mathbf{Z}\}$ , as shown in Figure 3.3.  $\mathbf{X}$  intercepts the equator and the prime meridian.  $\mathbf{Z}$  intercepts the north pole.  $\mathbf{Y}$  is defined as  $\mathbf{Z} \times \mathbf{X}$ .

$\mathcal{F}_g$  is the geographic coordinate frame located at the ground station, with orthonormal basis vectors  $\{\mathbf{D}, \mathbf{E}, \mathbf{N}\}$  where  $\mathbf{D}$  points down, perpendicular to the surface of the earth,  $\mathbf{E}$  point east, and  $\mathbf{N}$  points north. This is shown in Figure 3.4

$\mathcal{F}_{gA}$  is the coordinate frame associated with the ground station antenna, with orthonormal basis vectors  $\{\mathbf{x}_{gA}, \mathbf{y}_{gA}, \mathbf{z}_{gA}\}$ . The vector  $\mathbf{z}_{gA}$  points in the direction of the maximum gain of the antenna.  $\mathbf{y}_{gA}$  lies in the  $\mathbf{N} - \mathbf{E}$  plane and  $\mathbf{x}_{gA}$  points away from the Earth.

$\mathcal{F}_{gc}$  is the local geocentric coordinate frame of the spacecraft with orthonormal basis vectors  $\{\mathbf{s}_c, \mathbf{u}_c, \mathbf{t}_c\}$ . The vector  $\mathbf{u}_c$  points at geocenter. The vector  $\mathbf{s}_c$  is perpendicular to  $\mathbf{u}_c$  and lies in the orbital plane. The vector  $\mathbf{t}_c = \mathbf{s}_c \times \mathbf{u}_c$  points in the cross track direction.

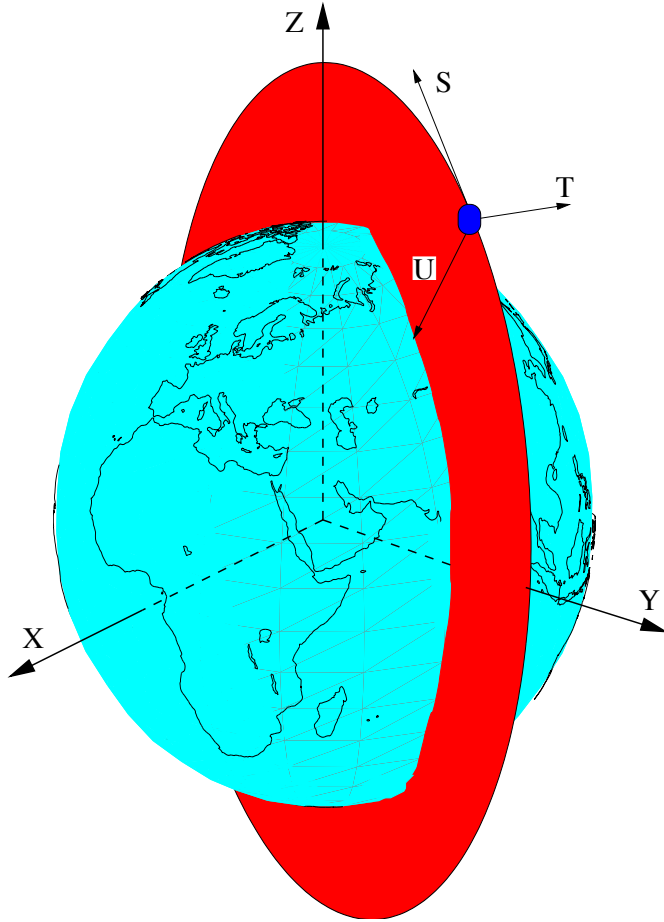


Figure 3.3: *Inertial and local coordinate frames. The inertial frame's basis vectors are  $\mathbf{X}, \mathbf{Y}$ , and  $\mathbf{Z}$  and its center is at the center of the earth. The spacecraft local coordinates frame has basis vectors  $\mathbf{S}, \mathbf{T}$ , and  $\mathbf{U}$ , centered at the spacecraft.*

$\mathcal{F}_{gd}$  is the local geodesic coordinate frame of the spacecraft with orthonormal basis vectors  $\{\mathbf{s}_d, \mathbf{u}_d, \mathbf{t}_d\}$ . The vector  $\mathbf{u}_d$  points at the earth, perpendicular to the surface. The vector  $\mathbf{s}_d$  is perpendicular to  $\mathbf{u}_d$  and lies in the orbital plane. The vector  $\mathbf{t}_d$  points in the cross track direction and is defined as  $\mathbf{t}_d = \mathbf{s}_d \times \mathbf{u}_d$ . Both local coordinate frames are depicted as  $\mathbf{S}, \mathbf{T}$  and  $\mathbf{U}$  in Figure 3.3.

$\mathcal{F}_b$  is the body coordinate frame, fixed in the body of the spacecraft. Its orthonormal basis vectors are  $\{\mathbf{x}_b, \mathbf{y}_b, \mathbf{z}_b\}$ . The origins of the local and body frames are collocated. The spacecraft local geodesic frame  $\mathcal{F}_{gd}$  differs from the spacecraft

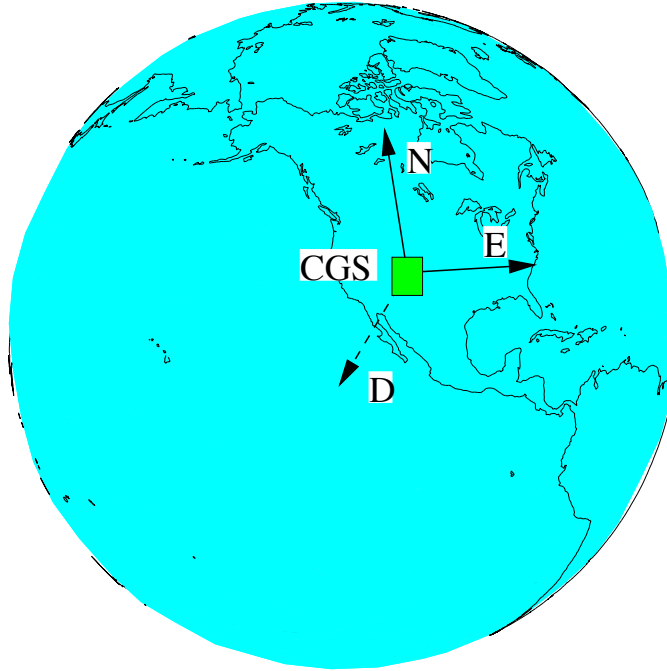


Figure 3.4: *Geographic coordinate frame.  $\mathbf{D}$  points down normal to the earth surface,  $\mathbf{E}$  and  $\mathbf{N}$  point north and east, respectively, both tangent to the earth surface.*

body frame  $\mathcal{F}_b$  by a sequential rotation about the  $S_d$ ,  $T_d$  and  $U_d$  axes. The rotation takes into account the attitude of the spacecraft, given by roll,  $\phi_R$ , pitch,  $\phi_P$  and yaw,  $\phi_Y$ . As shown in Figure 3.2,  $\phi_R$  is the rotation about  $\mathbf{s}_d$ ,  $\phi_P$  is the rotation about  $\mathbf{t}_d$ , and  $\phi_Y$  is the rotation about  $\mathbf{u}_d$ .

$\mathcal{F}_{sA}$  is the coordinate frame associated with the spacecraft antenna, with orthonormal basis vectors  $\{\mathbf{x}_{sA}, \mathbf{y}_{sA}, \mathbf{z}_{sA}\}$ . The vector  $\mathbf{z}_{sA}$  points in the direction of the maximum gain of the antenna, and the vectors  $\mathbf{x}_{sA}$  and  $\mathbf{y}_{sA}$  are defined by the antenna gain pattern.

### 3.2 Rotation Matrices

The following rotation matrices allow for the conversion of one coordinate frame to another. In this section,  ${}^y\mathcal{A}^x$  represents the rotation matrix used to convert a vector in  $\mathcal{F}_x$  to one in  $\mathcal{F}_y$ . Vectors are written in bold.

$[{}^{gc}\mathcal{A}^I](\mathbf{v}_s, \mathbf{r}_s)$ . The geocentric local coordinate system can be obtained by a rotation of axes of the inertial coordinate system. The rotation matrix is defined by Equation (3.3), where  $\mathbf{v}_s$  is the spacecraft velocity and  $\mathbf{r}_s$  is the position vector of the spacecraft,

$$[{}^{gc}\mathcal{A}^I] = \left( \frac{\mathbf{r}_s}{\|\mathbf{r}_s\|} \times \left( \frac{\mathbf{v}_s}{\|\mathbf{v}_s\|} \times \frac{\mathbf{r}_s}{\|\mathbf{r}_s\|} \right), \frac{\mathbf{v}_s}{\|\mathbf{v}_s\|} \times \frac{\mathbf{r}_s}{\|\mathbf{r}_s\|}, -\frac{\mathbf{r}_s}{\|\mathbf{r}_s\|} \right). \quad (3.3)$$

$[{}^{gd}\mathcal{A}^{gc}](\mathbf{r}_s)$ . The geodetic local coordinate system can be obtained by a rotation of axes of the geocentric local coordinate system. The rotation matrix is defined by

$$[{}^{gd}\mathcal{A}^{gc}] = \begin{pmatrix} \frac{\mathbf{ssn}}{\|\mathbf{ssn}\|} \cdot \mathbf{S}_c & \frac{\mathbf{ssn}}{\|\mathbf{ssn}\|} \cdot \mathbf{t}_c & \frac{\mathbf{ssn}}{\|\mathbf{ssn}\|} \cdot \mathbf{u}_c \\ \frac{\mathbf{ttn}}{\|\mathbf{ttn}\|} \cdot \mathbf{S}_c & \frac{\mathbf{ttn}}{\|\mathbf{ttn}\|} \cdot \mathbf{t}_c & \frac{\mathbf{ttn}}{\|\mathbf{ttn}\|} \cdot \mathbf{u}_c \\ \frac{\mathbf{uun}}{\|\mathbf{uun}\|} \cdot \mathbf{S}_c & \frac{\mathbf{uun}}{\|\mathbf{uun}\|} \cdot \mathbf{t}_c & \frac{\mathbf{uun}}{\|\mathbf{uun}\|} \cdot \mathbf{u}_c \end{pmatrix}, \quad (3.4)$$

where

$$\mathbf{ssn} = \mathbf{ttn} \times \mathbf{uun}$$

$$\mathbf{ttn} = \mathbf{uun} \times \mathbf{v}_s$$

$$\mathbf{uun} = r_l \begin{pmatrix} \cos(clat) \cos(clon) \\ \cos(clat) \sin(clon) \\ \sin(clat) - z_I \end{pmatrix} - [\mathbf{r}_s]^I$$

$$r_l = \text{local radius of the earth} = a \cdot (1 - FLAT \cdot \sin^2(clat))$$

$$clat = \text{appr. latitude of geodetic nadir} = \tan^{-1}((1 - e^2) \cdot \tan(xlat))$$

$$clon = \text{longitude of nadir}$$

$$xlat = \text{geocentric latitude of geocentric nadir}$$

$$a = \text{semimajor axis of the earth}$$

$$FLAT = \text{flatness constant of the earth}$$

$$e = \text{eccentricity of the earth.}$$

$[{}^b\mathcal{A}^{gd}] (\phi_R, \phi_P, \phi_Y)$ . The geodetic coordinate system can be converted to the spacecraft body coordinate system by applying the appropriate roll, pitch and yaw to the following rotation matrix,

$$[{}^b\mathcal{A}^{gd}] = \begin{pmatrix} \cos(\phi_Y) & -\sin(\phi_Y) & 0 \\ \sin(\phi_Y) & \cos(\phi_Y) & 0 \\ 0 & 0 & 1 \end{pmatrix} \begin{pmatrix} \cos(\phi_P) & 0 & \sin(\phi_P) \\ 0 & 1 & 0 \\ -\sin(\phi_P) & 0 & \cos(\phi_P) \end{pmatrix} \begin{pmatrix} 0 & 0 & 1 \\ 0 & \cos(\phi_R) & -\sin(\phi_R) \\ 0 & \sin(\phi_R) & \cos(\phi_R) \end{pmatrix}. \quad (3.5)$$

$[{}^{sA}\mathcal{A}^b] (\theta_A, \phi_A)$ . The spacecraft antenna coordinate system can be obtained by a rotation of  $\phi_A^\circ$  about the  $\mathbf{z}_b$  axis, then a rotation of  $\theta_A^\circ$  ( $40^\circ$  for the inner beam or  $46^\circ$  for the outer beam) about the  $\mathbf{y}_b$  axis of the body coordinate system,

$$[{}^{sA}\mathcal{A}^b] = \begin{pmatrix} \cos(\theta_A) & 0 & \sin(\theta_A) \\ 0 & 1 & 0 \\ -\sin(\theta_A) & 0 & \cos(\theta_A) \end{pmatrix} \begin{pmatrix} \cos(\phi_A) & -\sin(\phi_A) & 0 \\ \sin(\phi_A) & \cos(\phi_A) & 0 \\ 0 & 0 & 1 \end{pmatrix} \quad (3.6)$$

where  $\phi_A$  and  $\theta_A$  are the azimuth and elevation angles, respectively, of  $\mathbf{r}_s - \mathbf{r}_g$  in the body coordinate frame.

$[{}^g\mathcal{A}^I] (\psi_{lat}, \psi_{lon})$ . The geographic coordinate system can be obtained by a  $\psi_{lon}$  degree rotation about the  $\mathbf{z}_I$  axis and then a  $-(90 + \psi_{lat})$  degree rotation about  $\mathbf{y}_I$ , where  $\psi_{lon}$  and  $\psi_{lat}$  are the geodetic longitude and latitude of the ground station, respectively, as defined by

$$[{}^g\mathcal{A}^I] = \begin{pmatrix} \cos(90 + \psi_{lat}) \cos(\psi_{lon}) & \cos(90 + \psi_{lat}) \sin(\psi_{lon}) & \sin(90 + \psi_{lat}) \\ -\sin(\psi_{lon}) & \cos(\psi_{lon}) & 0 \\ -\sin(90 + \psi_{lat}) \cos(\psi_{lon}) & -\sin(90 + \psi_{lat}) \sin(\psi_{lon}) & \cos(90 + \psi_{lat}) \end{pmatrix}. \quad (3.7)$$

$[{}^{gA}\mathcal{A}^g] (\phi_g, \theta_g)$ . The ground station antenna coordinate system can be obtained by a rotation of  $\phi_g$  about the  $\mathbf{z}_g$  axis, then a rotation of  $\theta_g$  about the  $\mathbf{y}_g$  axis

of the geographic coordinate system, where  $\theta_g$  is the elevation angle and  $\phi_g$  is the azimuth angle of  $\mathbf{r}_g - \mathbf{r}_s$  in the geographic coordinate frame,

$$[{}^g\mathcal{A}^g] = \begin{pmatrix} \cos(\theta_g) & 0 & \sin(\theta_g) \\ 0 & 1 & 0 \\ -\sin(\theta_g) & 0 & \cos(\theta_g) \end{pmatrix} \begin{pmatrix} \cos(\phi_g) & -\sin(\phi_g) & 0 \\ \sin(\phi_g) & \cos(\phi_g) & 0 \\ 0 & 0 & 1 \end{pmatrix}. \quad (3.8)$$

Using the rotation matrices, a vector in the inertial coordinate system can be converted to the spacecraft antenna coordinate system and the ground station coordinate system by the following equations,

$$[\mathbf{R}]^{sA} = [{}^{sA}\mathcal{A}^b] [{}^b\mathcal{A}^{gd}] [{}^{gd}\mathcal{A}^{gc}] [{}^{gc}\mathcal{A}^I] [\mathbf{R}]^I \quad (3.9)$$

and

$$[\mathbf{R}]^{gA} = [{}^g\mathcal{A}^g] [{}^g\mathcal{A}^I] [\mathbf{R}]^I, \quad (3.10)$$

where

$$[\mathbf{R}] = \begin{pmatrix} r_x & r_y & r_z \end{pmatrix}^T.$$

The spacecraft and ground station antenna gain patterns shown in Figures 3.5 and 3.6 are measured and entered into lookup tables which are indexed by two parameters:  $\Theta$ , the azimuth angle from boresight, and  $\Phi$ , the elevation angle from boresight. To find the antenna gain in the direction of a vector  $\mathbf{r}$  that is resolved in the coordinate frame of the antenna, the following equations are used:

$$\Theta = \tan^{-1} \left( \frac{\sqrt{r_x^2 + r_y^2}}{r_z} \right) \quad (3.11)$$

$$\Phi = \tan^{-1} \left( \frac{y_z}{x_z} \right). \quad (3.12)$$

### 3.3 Results

In order to present sample results from the geometry calculations, let us consider a simulated mid latitude pass as shown in Figure 3.7. This represents a likely scenario of the satellite in relation to the CGS in actual operation.

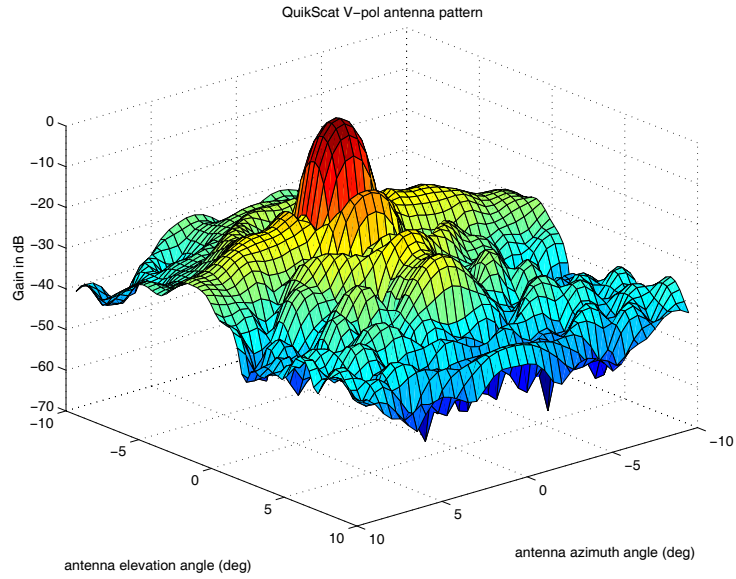


Figure 3.5: *Spacecraft antenna pattern. The narrow main beam is designed to enhance the resolution of the scatterometer measurements.*

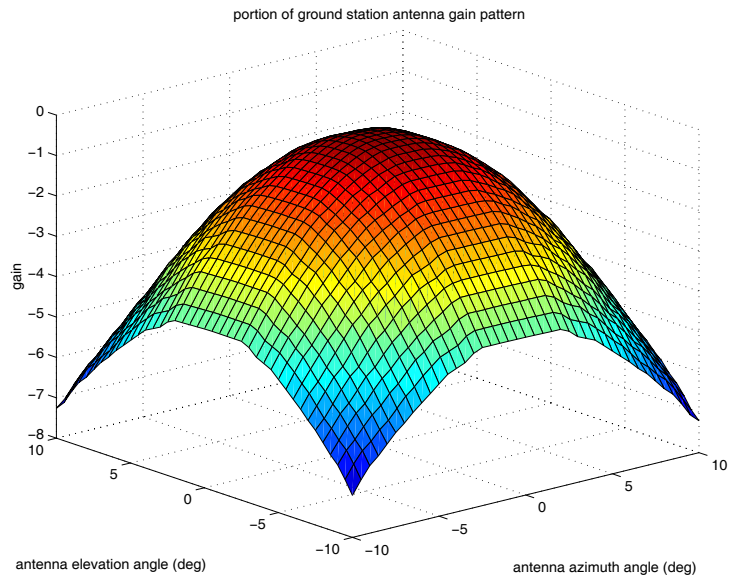


Figure 3.6: *CGS antenna pattern. It was designed with a wide main beam to minimize power variations due to alignment during data capture. (See also Fig. 5.8)*

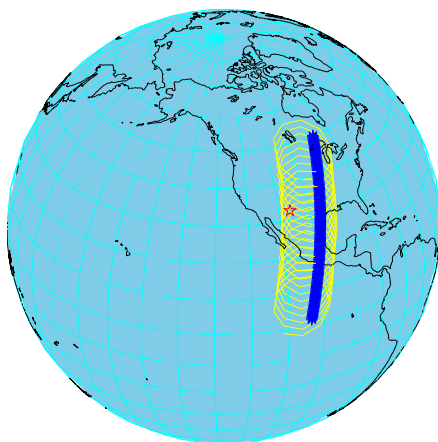
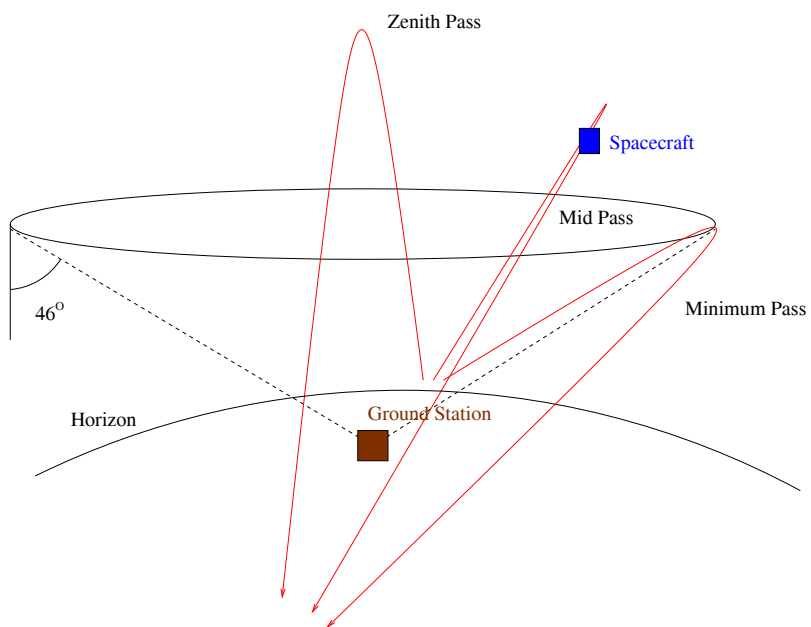


Figure 3.7: Visual representation of a mid latitude pass. The top figure compares the mid pass to a zenith pass and a min pass. The bottom figure shows the satellite path (dark asterisks), the footprint trace (light helical pattern) and the CGS location (star) during a mid pass.

The calculated range,  $|\mathbf{r}_s|$ , and Doppler effect,  $f_{dop}$ , of the satellite with respect to the CGS are shown in Figure 3.8. The minimum of the range curve is marked by an asterisk. This represents the point at which the satellite is closest to the CGS and starts to recede instead of approach. It also marks the point at which the relative velocity with respect to the CGS is zero and therefore the Doppler effect is also zero. Over a smaller window of time, such as a ten second period like those captured by the CGS, the Doppler effect appears linear, as shown in Figure 3.9.

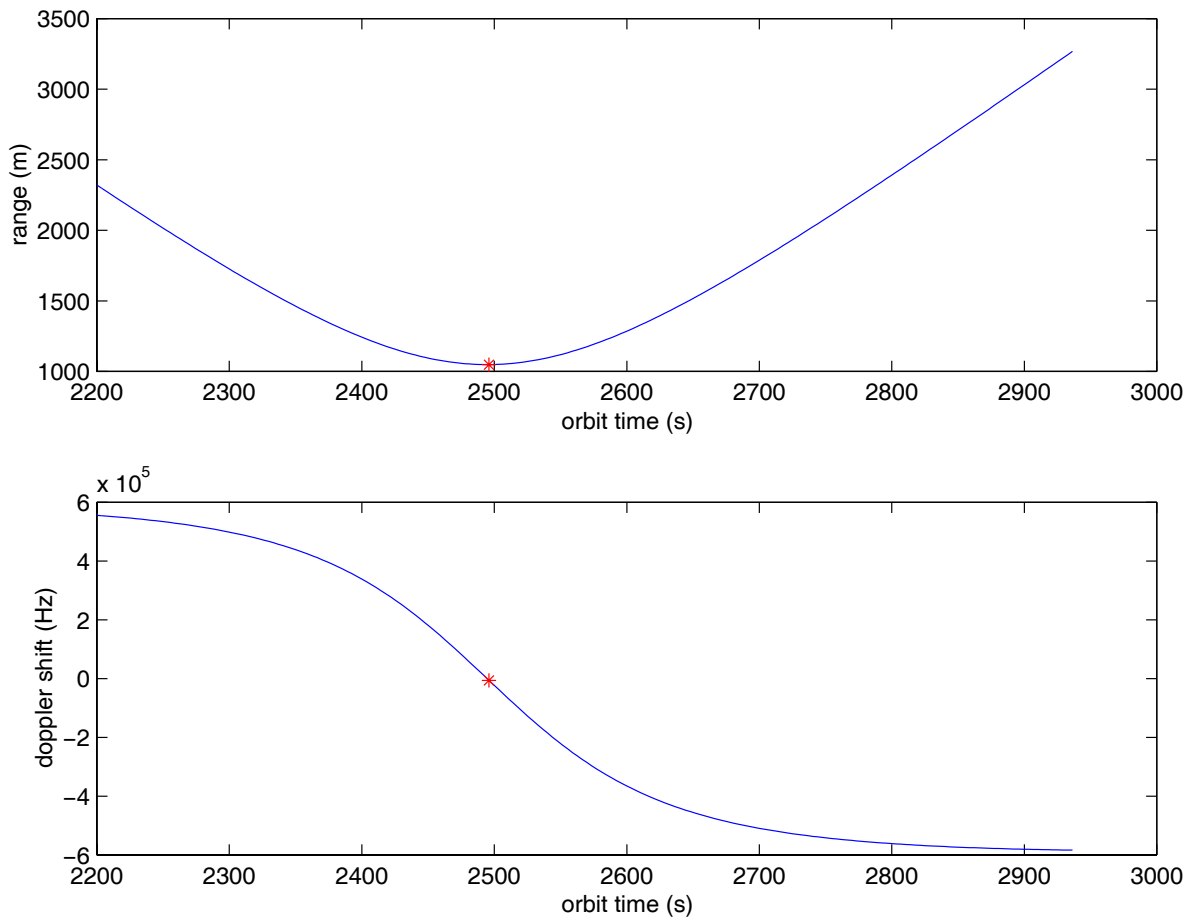


Figure 3.8: *Range and Doppler between satellite and CGS during a mid pass. The asterisk indicates the point of closest proximity.*

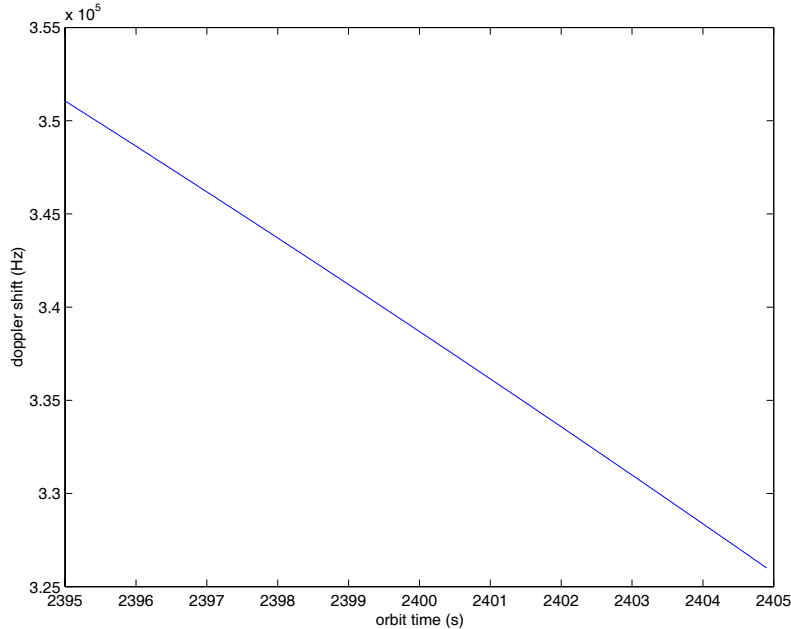


Figure 3.9: *Doppler frequency during time of CGS capture. Over the ten second interval, the Doppler effect is nearly linear.*

The SeaWinds and CGS antenna gains over a sixty second window during the simulated midpass are shown in Figures 3.10 and 3.11. The variation within the SeaWinds antenna gain comes mainly from the azimuthal rotation of the antenna. At each different azimuth angle, the vector connecting the CGS and the SeaWinds antenna pierces the antenna pattern at a different location. The variation within the ground station antenna gain, on the other hand stems from the movement of the satellite across the sky. At each different satellite location, the vector connecting QuikSCAT with the CGS pierces the CGS antenna pattern at a different location. The differences between the two antenna patterns are highlighted by this example. The CGS antenna was designed with a wide main beam so as to minimize the gain variation over the time of capture. The SeaWinds antenna, on the other hand, was designed with a narrow main beam to reduce the effective footprint size and therefore increase the resolution of the scatterometer. This results in wide power variations in the CGS data which is the basis of the CGS power analysis.

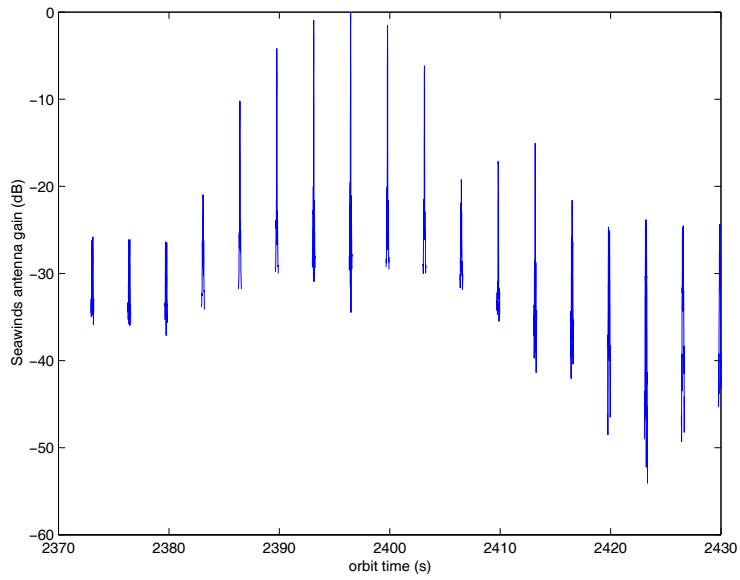


Figure 3.10: *Simulation of SeaWinds antenna gain over a sixty second capture. The data segments represent azimuth slices through the antenna pattern. See text for more details.*

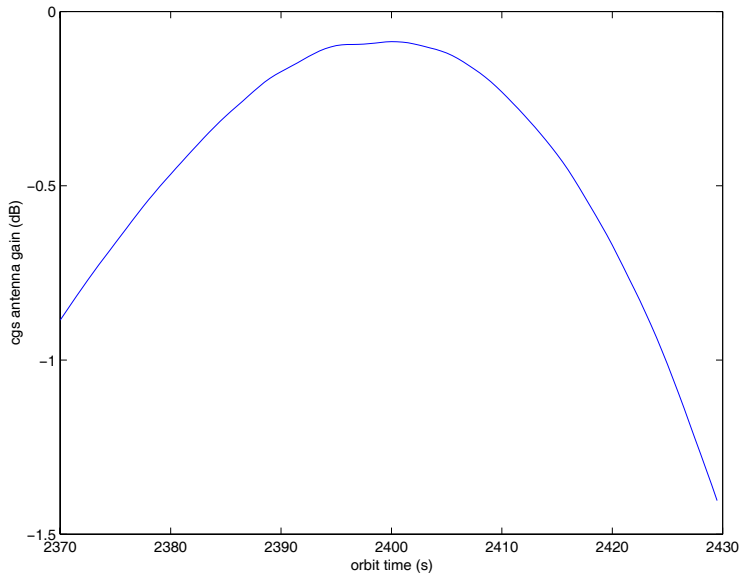


Figure 3.11: *CGS antenna gain over a sixty second simulated capture. Variation occurs due to satellite's displacement during capture.*

The intervals with no data are ones in which the vector  $(\mathbf{r}_s - \mathbf{r}_g)$  in the antenna pattern coordinate frame points outside of the known, tabulated  $10^\circ \times 10^\circ$  antenna pattern field. The peaks of the segments of data trace out elevation slices through the antenna pattern. Over a ten second interval, such as a CGS capture, the CGS receives only three segments of data, or sweeps, as shown in Figure 3.12.

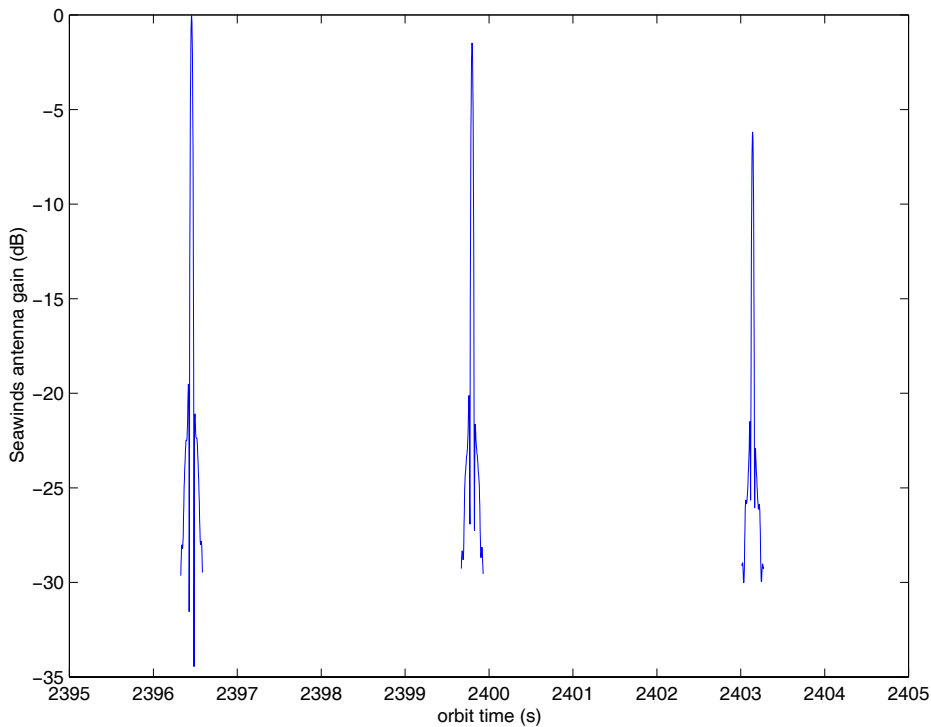


Figure 3.12: *Simulated ten second capture of CGS data. Three segments of data represent three sweeps caused by three rotations of the SeaWinds antenna during the time of capture. (See also Fig. 3.10)*

Each sweep traces out an azimuth slice through the antenna pattern. The data in Figure 3.12, for instance, shows three sweeps that slice through the main beam of the antenna pattern. Plotting the received power with respect to the calculated antenna elevation and azimuth angles, results in a partial reconstruction of the antenna pattern, as shown in Figure 3.13. Ideally, the power data corresponds exactly

with the known antenna pattern, as shown in Figure 3.14. Errors in position, attitude or timing cause the transmitted signal to cross the antenna pattern at locations other than those calculated and therefore cause the data to be misaligned. Figuring out which perturbations cause the misalignment is the basic task of the CGS power analysis.

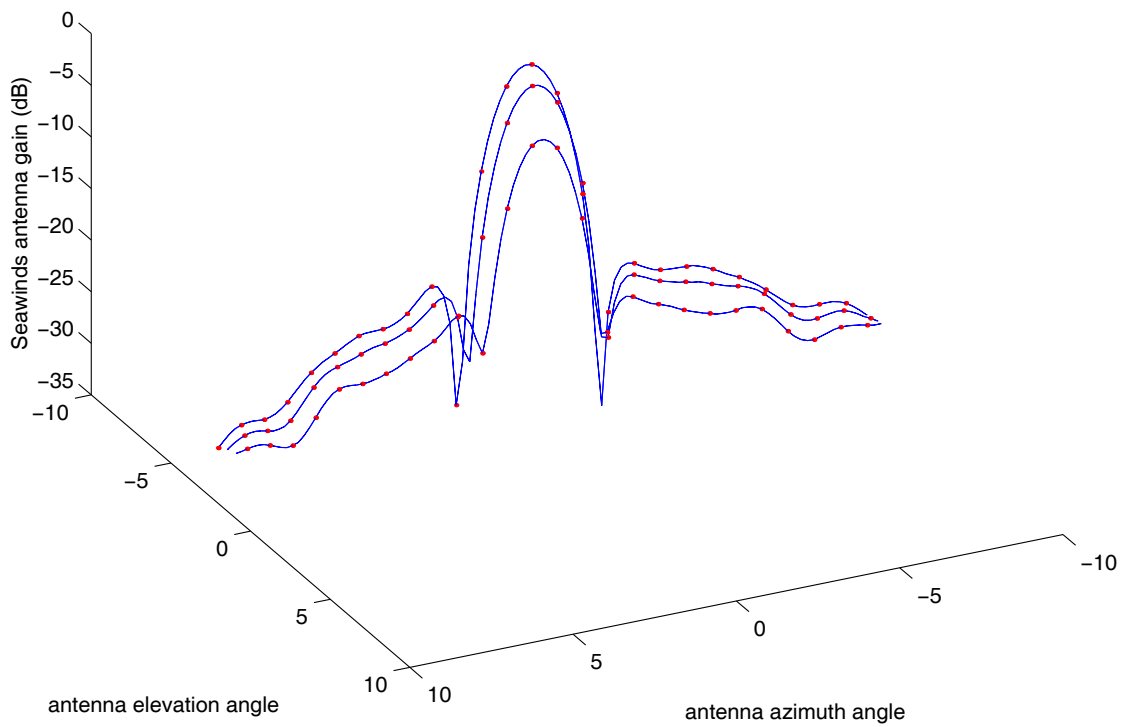


Figure 3.13: *Simulated data during ten second capture plotted against antenna azimuth and elevation angles. The result is a partial reconstruction of the antenna pattern.*

QuikScat V-pol antenna pattern

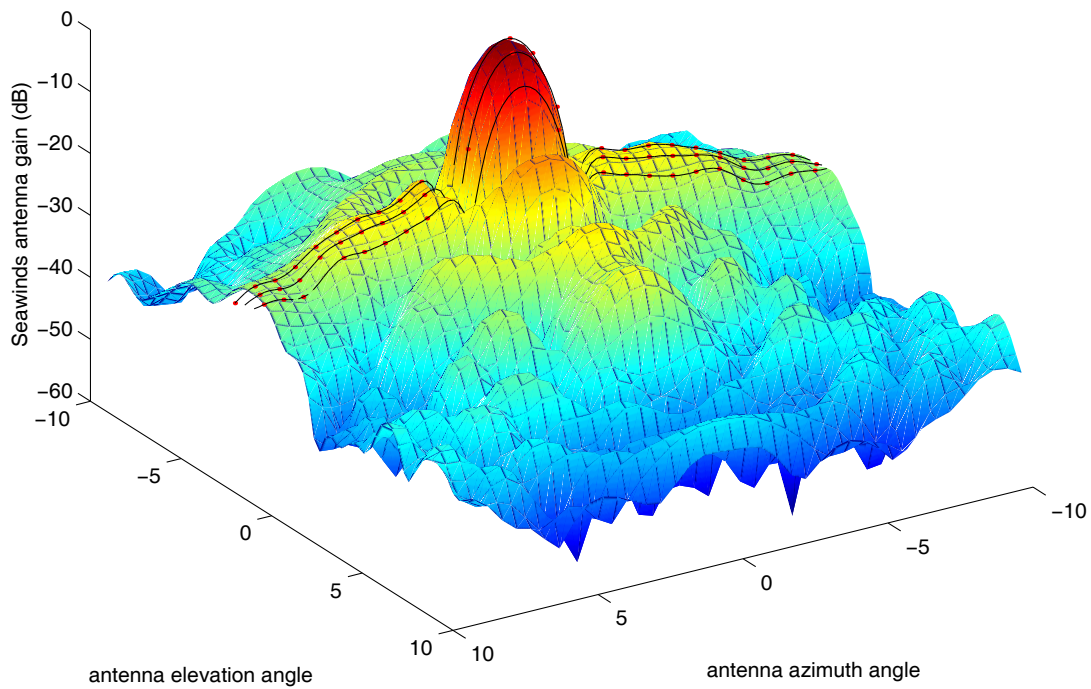


Figure 3.14: *Simulated data from Figure 3.13 plotted atop the antenna pattern. Ideally, the two align. The CGS power analysis estimates the causes of misalignments.*

## Chapter 4

### Sensitivity Analysis

The purpose of the QuikSCAT Calibration Ground Station (CGS) is to receive the transmitted signal of Seawinds on QuikSCAT as the instrument illuminates the CGS and its surrounding area. The principle use of the CGS data is to calibrate the satellite's position, attitude, and timing. The concept behind the calibration of these parameters is to compute the ideal expected signal and to compare it to the actual received signal, assuming that the differences between the two signals are caused by perturbations in the parameters. One requirement for this calibration method is that the two signals, the calculated expected and the actual received, must be identifiable. If perturbations in position, attitude, or timing do not produce a change in the amplitude or frequency of the received signal, there is little hope in using the CGS effectively to calibrate the parameters in question.

This chapter describes an analysis which calculates the change in the CGS data caused by perturbations of the parameters, i.e. to determine the sensitivity of the signal to perturbations in position, attitude and timing.

#### 4.1 Analysis Method

The main element of the sensitivity analysis is the accurate simulation of the operation of the QuikSCAT satellite. A key tool used in the simulation is a software orbit propagation program, provided by Jet Propulsion Laboratory (JPL). The orbit propagator, entitled `scstate`, calculates the satellite's position and velocity according to a user entered orbit time, given a starting point and the proper orbit parameters.

The orbit parameters which most accurately describe the anticipated QuikSCAT orbit are listed in Table 4.1.

Table 4.1: *QuikSCAT Orbit Parameters*

Eccentricity	0.0001425
Inclination Angle	98.6267°
Longitude of Ascending Node	255.8351°
Argument of Perigee	76.9019
Semi-Major Axis	7181.048 km

As described in Chapter 3, geometry calculations use the satellite’s calculated position and velocity to compute the power and frequency of the signal received at the CGS for any time during a particular simulated pass. The sensitivity analysis consists of multiple simulations, mimicking the reception of both the inner and outer beam for three different types of passes, namely a minimum pass, a mid pass and a zenith pass, as shown in Figure 3.7. This analysis does not take sensor noise into account.

For each different type of pass, the received signal is simulated a number of times, first with nominal position, attitude and timing, followed by simulations with pertinent parameters perturbed individually. The analysed perturbations include error along  $\mathbf{S}$ , error along  $\mathbf{T}$ , and error along  $\mathbf{U}$ , roll, pitch and yaw (all as defined in Chapter 3), as well as antenna angular position and absolute time error.

Each of the perturbations is simulated by adjusting the input parameters of the simulation to be different than those of the corresponding nominal pass. A nominal pass assumes perfect attitude, for instance. Simulating a roll of  $0.1^\circ$  requires an input roll of  $0.1^\circ$  while leaving all other parameters as their nominal values. Likewise, the pitch and the yaw are perturbed by adjusting the input pitch or yaw and leaving all other parameters as their nominal values.

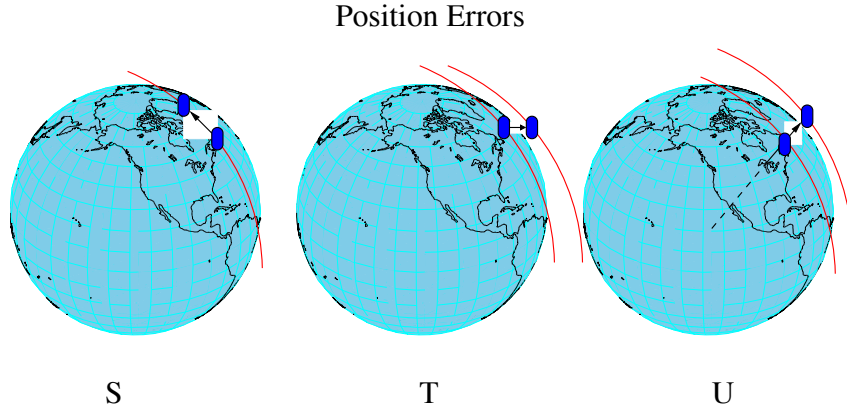


Figure 4.1: *Visual depiction of position errors along  $\mathbf{S}$ ,  $\mathbf{T}$ , and  $\mathbf{U}$  axes.*

Perturbing the position error is not quite as straightforward as perturbing the attitude and is accomplished by the following approximations. The error along  $\mathbf{S}$  is perturbed by adjusting the orbit time so that the satellite is positioned closer or further along its orbit track. Increasing the orbit time not only moves the satellite further along its path, but also causes the antenna to rotate slightly. This antenna rotation is not desired in the  $\mathbf{S}$  error perturbation, and is compensated for by readjusting the initial azimuth angle. The error along  $\mathbf{T}$  is perturbed by adjusting the longitude of the ascending node if the pass. This effectively rotates the earth underneath the satellite. Increasing the longitude places the satellite further east and therefore in the positive  $\mathbf{T}$  direction, whereas decreasing the initial longitude places it further west and therefore shifts it in the negative direction. The error along  $\mathbf{U}$  is perturbed by adjusting the semi-major axis of the orbit. This changes the altitude of the spacecraft and thereby moves it along the  $\mathbf{U}$  axis. The position errors are depicted in Figure 4.1.

The analysis could be changed to compute the exact direction of the  $\mathbf{S}$ ,  $\mathbf{T}$ , and  $\mathbf{U}$  axes and precisely reposition the satellite to simulate the desired perturbation, but would require extensive modification of the existing routines. For the purpose of this sensitivity analysis, the approximations suffice, based on back of the envelope calculations.

The antenna angular position is perturbed by adjusting the initial antenna azimuth angle. Likewise, the absolute time error is perturbed by adjusting the initial orbit time. Increasing the orbit time moves the satellite further and rotates the antenna, so it basically couples the perturbation along  $\mathbf{S}$  with antenna angular position perturbation.

## 4.2 Initial Sensitivity Results

One of the first items of interest from the sensitivity analysis is the difference in gain between the received signal from a nominal pass and the received signal from a perturbed pass. Figure 4.2 shows the results of the analysis of the error along  $\mathbf{T}$ .

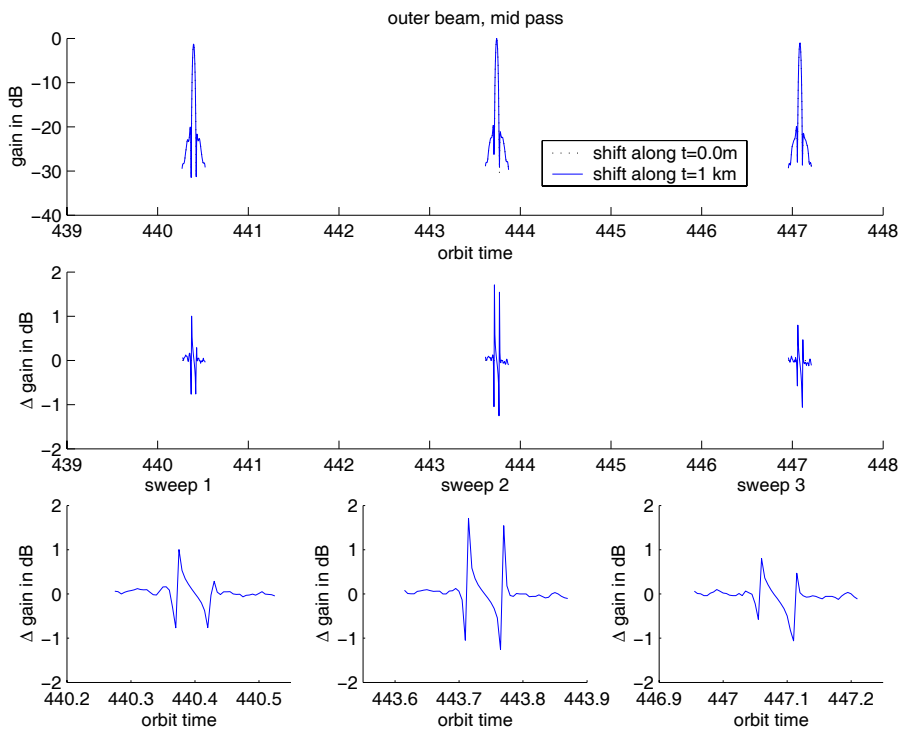


Figure 4.2: *Gain and gain difference for position errors along the  $\mathbf{T}$  axis for a mid pass. The top graph shows the received signal for both a nominal approaching mid pass and an approaching mid pass with a simulated position error of 1 km along the  $\mathbf{T}$  axis. The dotted curve is barely discernible due to its similarity with the solid curve. The middle graph shows the gain difference between the two. The bottom graphs show closeups of the error during the three consecutive sweeps.*

Results such as those shown in Figure 4.2 provide a maximum difference value for each perturbation as well as the shape of the difference between the nominal data and the perturbed data, which could act as a signature for each perturbation. Although this provides an initial feel for the sensitivity of the received signal to perturbations, the maximum gain difference occurs at the nulls between the main beam and the first sidelobes. This number is highly dependent upon sampling and timing and thus an unreliable metric.

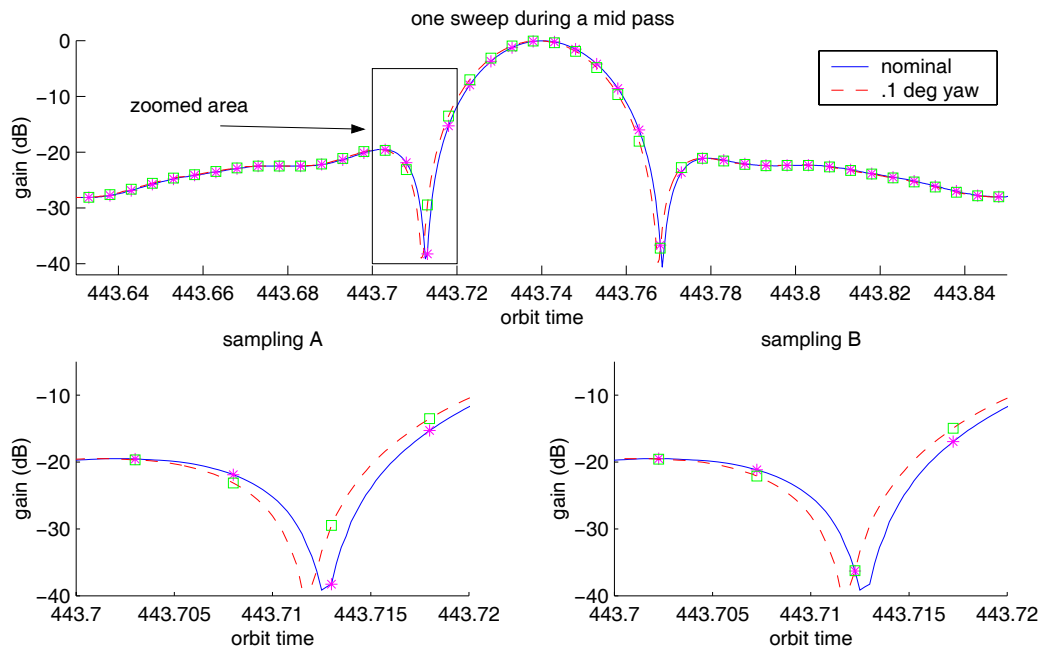


Figure 4.3: *Demonstration of sampling ambiguity. The top graph shows the gains for a nominal sweep across the CGS during a simulated mid pass and the corresponding sweep with a yaw bias of  $0.1^\circ$ . The bottom two graphs show possible pulse locations. Pulses are spaced approximately 5 ms apart. The difference between sampling A and sampling B lies only in the timing of the initial pulse.*

As the antenna rotates, the signal that travels in the direction of the CGS slices through a certain portion of the SeaWinds antenna pattern. The main effect of perturbations is a change in the location of the antenna pattern slice. If the timing

of the pulses is such that the antenna pattern slice is sampled right at the null in the nominal pass and the corresponding pulse is found along the main beam in the perturbed pass, the difference between the two will be large. If, on the other hand, the two different samplings straddle the null, their difference will be considerably smaller than they would in the first case. Thus, for the same set of antenna slices, sampling, or the timing of pulses could make the difference between a maximum gain difference of 10 dB and a maximum gain difference of 0.1 dB, as shown in Figure 4.3.

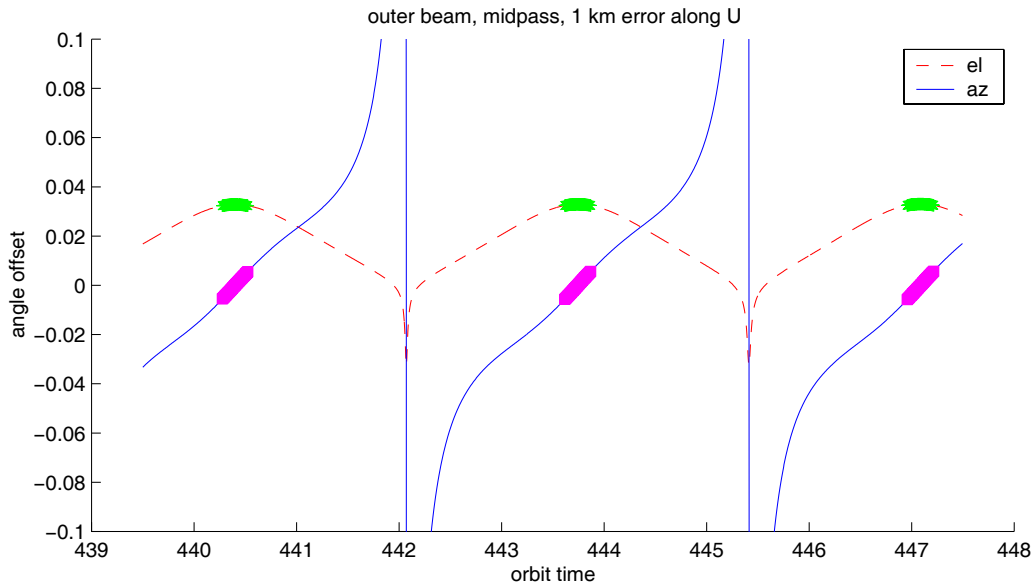


Figure 4.4: *Angle difference for position errors along the  $\mathbf{U}$  axis for a mid pass. The dashed line and solid line represent the elevation and azimuth angle differences, respectively, between the slices through the antenna pattern for three sweeps of a nominal pass and a pass with a 1 km position bias along the  $\mathbf{U}$  axis. The highlighted portions of the curves represent the series of pulses that occur when the CGS is illuminated, i.e. when the antenna is pointed toward the CGS. The plot shows that for a mid pass with a position error along  $\mathbf{U}$ , the elevation error is much larger than the azimuth error from the perspective of the CGS.*

### 4.3 Improved Presentation of Results

An alternative measure of the sensitivity of the received signal to perturbations is the movement of the slice through the antenna pattern as a result of the perturbations. This statistic, unlike the maximum gain difference, is independent of the timing and sampling of the pulses. Figure 4.4 shows the elevation and azimuth angle offset within the antenna pattern for a mid pass due to a position error along the **U** axis. Figure 4.5 shows the same angle offsets for a minimum, a mid and a zenith pass due to a  $0.1^\circ$  roll bias.

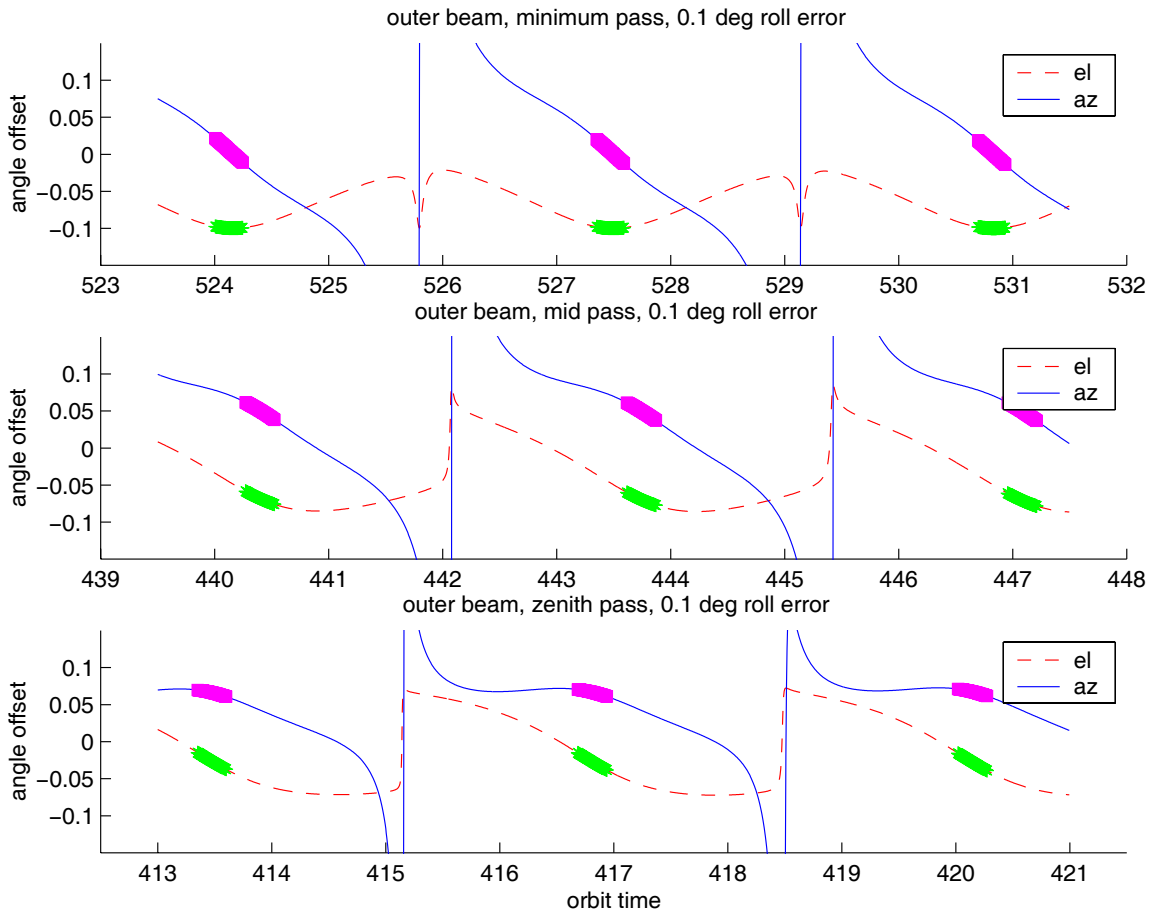


Figure 4.5: Angle offsets for outer beam,  $0.1^\circ$  roll error. Results for a minimum pass, a mid pass and a zenith pass are combined into one figure for comparison.

The results shown in Figure 4.5 are more clearly illustrated in Figure 4.6. Figures 4.7 and 4.8 show compilations of the results for all analyzed perturbations and all passes. See captions for explanations of each figure.

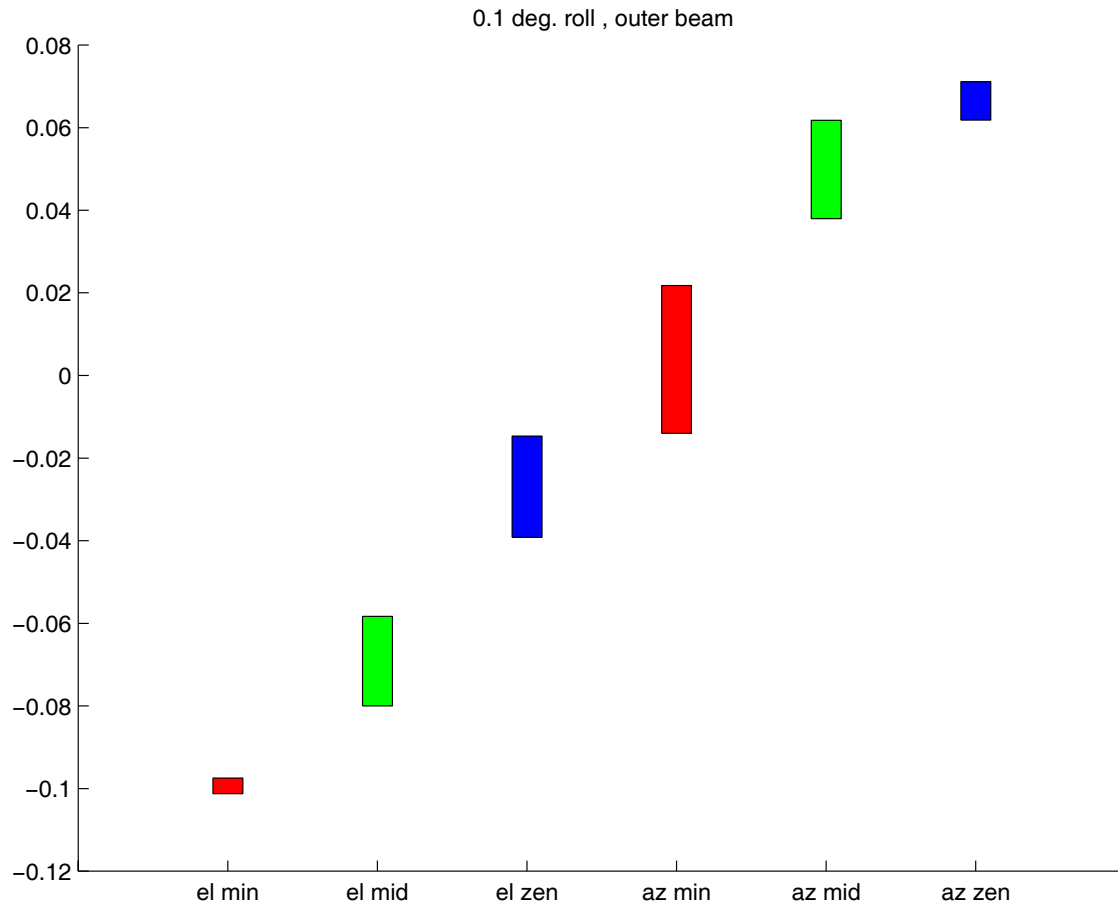


Figure 4.6: *Concise sensitivity results for outer beam, 0.1° roll. Each bar represents the range of expected angle offset for a 0.1° roll bias during the reception of a given pass. The magnitude of the azimuth angle offset increases from a minimum pass to a mid pass to a zenith pass. The value of the elevation angle offset increases while its magnitude decreases from a minimum to a mid to a zenith pass. These trends act as a signature for the roll perturbation.*

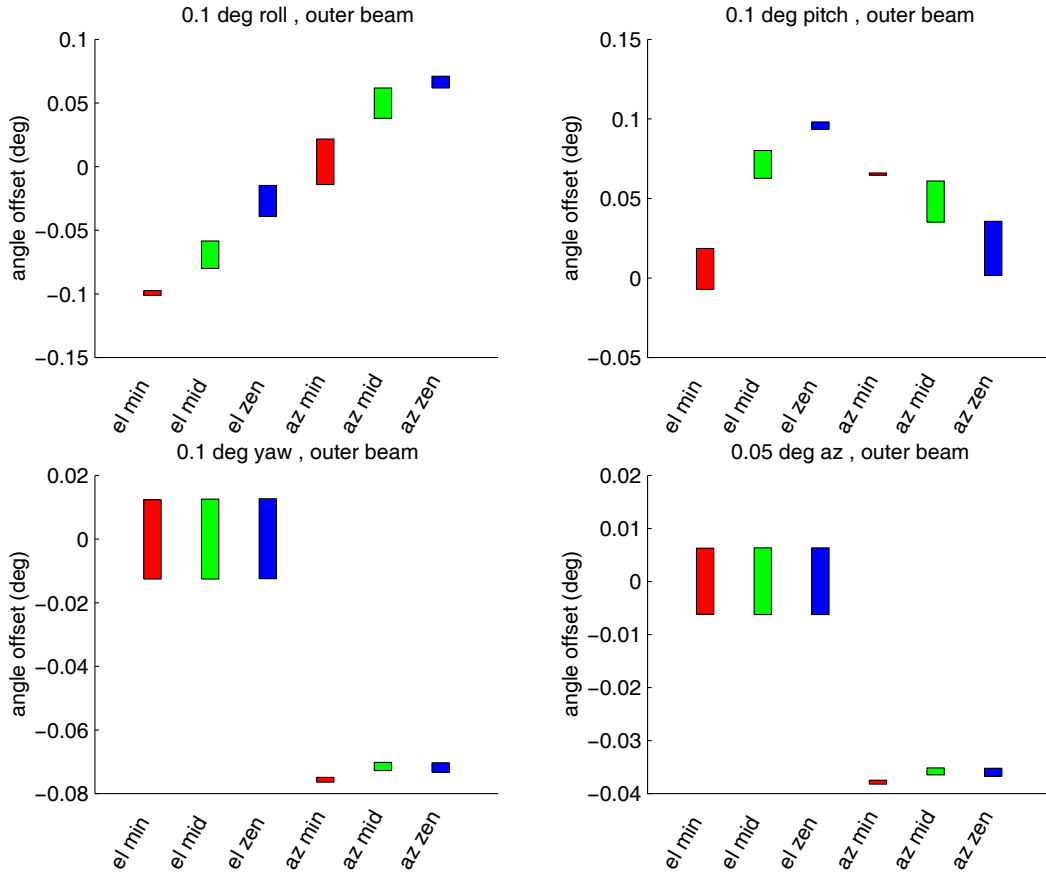


Figure 4.7: *Summary of sensitivity analysis results for roll, pitch, yaw and antenna azimuth. Roll, pitch and yaw cause distinct sets of angle offsets for each type of pass (min, mid, zenith). Yaw and antenna azimuth yield similar results. This means that separating yaw errors from antenna azimuth errors in CGS data requires more than elevation and azimuth angle offsets. These results are representative of those obtained for the inner beam simulation, as well as the outer beam simulation.*

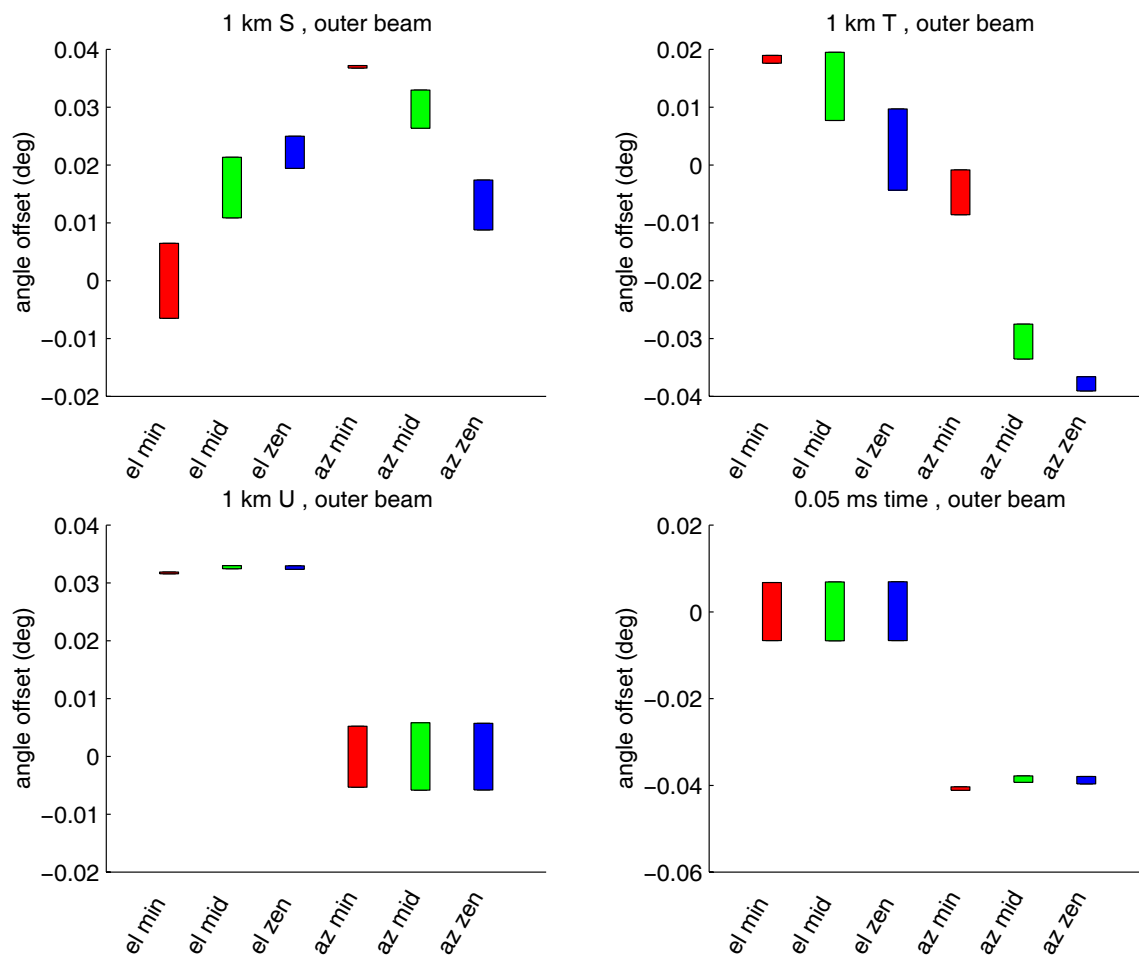


Figure 4.8: Summary of sensitivity analysis results for shifts along **S**, **T**, and **U** and for a timing shift. Shifts along **S**, **T**, and **U** cause distinct sets of angle offsets for each type of pass (min, mid, zenith). The results from a timing shift are very similar to those caused by yaw and antenna azimuth shifts. Perturbations yielding similar errors are difficult to separate in CGS data. These results are representative of those obtained for the inner beam simulation as well as the outer beam simulation.

#### 4.4 Conclusion

The results shown in Figures 4.7 and 4.8 offer a comprehensive view of the sensitivity of the received signal at the ground station to perturbations in the attitude, position and timing of the spacecraft. They show that position errors of 1 km or attitude errors of  $0.1^\circ$  can shift the vector pointing from the spacecraft to the CGS by up to  $0.1^\circ$  within the antenna pattern. This can translate into a gain difference of possibly 2 dB along the main beam of the antenna pattern.

The results also suggest a method to deduce, or initially estimate, position or attitude errors from the CGS data. The combination of antenna pattern angle errors caused by each perturbation serves as a signature for that particular perturbation. If, for instance, the CGS data shows a consistent elevation angle offset of around  $0.01^\circ$  and a consistent azimuth angle offset of around  $0.07^\circ$  within the antenna pattern, a yaw bias of  $0.1^\circ$  is a possible cause. By the same token, if the CGS data indicates an elevation error which decreases the higher the spacecraft cuts across the sky (i.e. larger for a minimum pass and smaller for a zenith pass) and an azimuth error which exhibits the opposite behavior (i.e. smaller for a minimum pass and larger for a zenith pass), then a roll bias may be a possible cause.



## Chapter 5

### Multipath Analysis

As mentioned in Chapter 2, the CGS receives the signal of the satellite as it passes overhead and illuminates the receiving antenna of the ground station. Ground processing uses the received signal to calibrate the attitude, position and timing of the satellite.

Noise may affect the integrity and usefulness of the received signal. Some possible sources of noise are atmospheric conditions, temperature inconsistencies and multipath. Multipath occurs when portions of the satellite signal scatter off of the CGS surroundings and are indirectly received by the antenna, as shown in Figure 5.1. This multipath may lead to power and/or timing errors in the measurement. This chapter documents the Calibration Ground Station multipath simulation, which provides an initial evaluation of the effects of multipath on the received signal.

Simulating multipath can be an extensive and computationally intensive task. In order to limit the complexity of this analysis, a key assumption has been made: the satellite signal bounces no more than once before reaching the receiving antenna. This effectively concludes that if the signal bounces more than once, its strength is small enough to neglect.

This assumption allows us to model the multipath as a collective reradiation of the transmitted signal off of the surroundings of the CGS. The surroundings of the CGS can be classified into three different groups. The first of these groups is the large-scale surrounding terrain. This includes all of the ground within sight of the CGS. As will be shown later, the further away the signal bounces off of the ground, the weaker its effect on the ground station signal. Thus, there is a cutoff distance

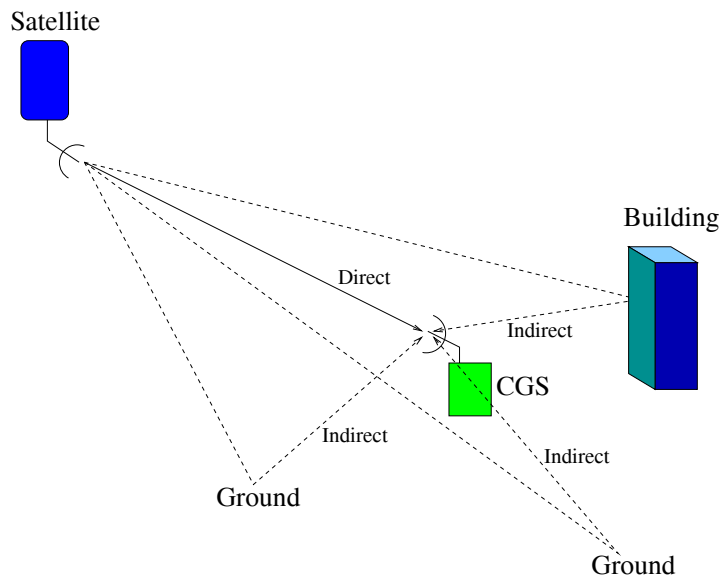


Figure 5.1: *Visualization of multipath. The transmitted signal bounces off of the surroundings of the receiver and arrives at a later time, out of sync with the directly received signal.*

and the ground beyond this is neglected in this analysis. The second group is the neighboring buildings. All of the buildings, walls and large objects in the vicinity of the CGS belong to this group. The third and last group is the CGS roof features. This includes the corrugated roof of the ground station, the lightning rods attached to the roof, as well as the radome cover of the antenna. Multipath caused by the roof is not investigated in this work. This analysis considers the multipath caused by the first two groups, the surrounding terrain and buildings.

The multipath analysis is a three part process. The first part of the analysis is the discretization of the scatterers. This includes a site survey and the discretization of the terrain and buildings into individual surface patches. The second part is the geometry analysis. This considers each of the surface patches and computes important geometrical parameters. The third part is an interference strength analysis, which computes the strength of the reradiated signal from each surface patch and adds them all up to determine the total multipath interference strength and compares it to the strength of the desired, directly received signal.

## 5.1 Discretization of Scatterers

In March of 1999, two research students, Arden Anderson and Peter Yoho, from BYU visited the CGS at the White Sands testing facility. There, under the direction of Jim Lux, an engineer from JPL, they carefully surveyed the area surrounding the CGS. They determined the location of all of the buildings and other prominent features, such as parking lots and water reservoirs, in the vicinity of the CGS.

To familiarize the reader with the surroundings of the CGS, Figure 5.2 shows a portion of the area. Manipulating the data collected from the site survey yields a simple electronic map of the area. After discretizing the buildings and other features into 62 individual triangular patches, the data is summarized as shown in Figure 5.3. The points that define the triangular surfaces each have a particular height, giving each surface its appropriate tilt.

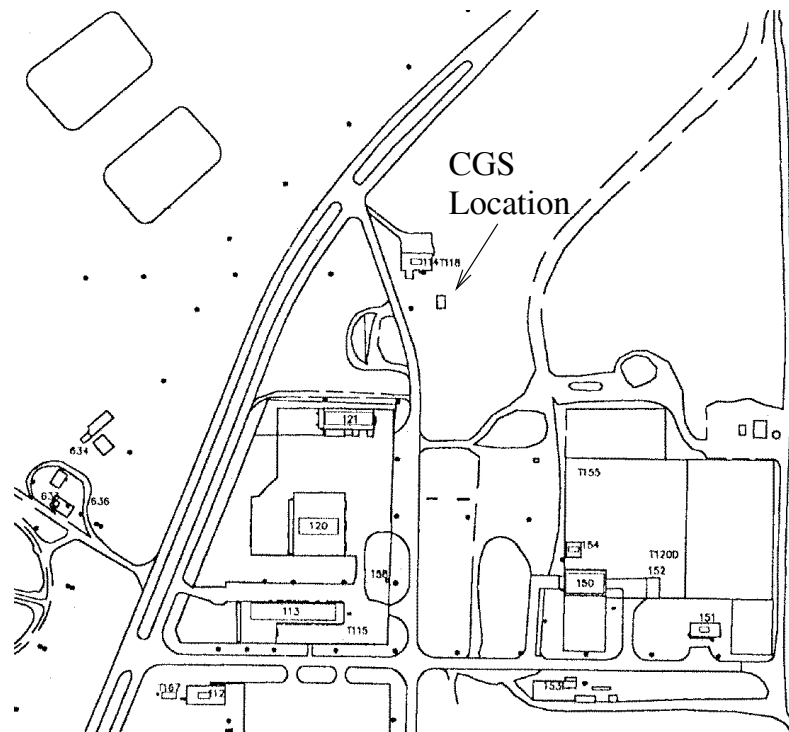


Figure 5.2: *CGS site map.*

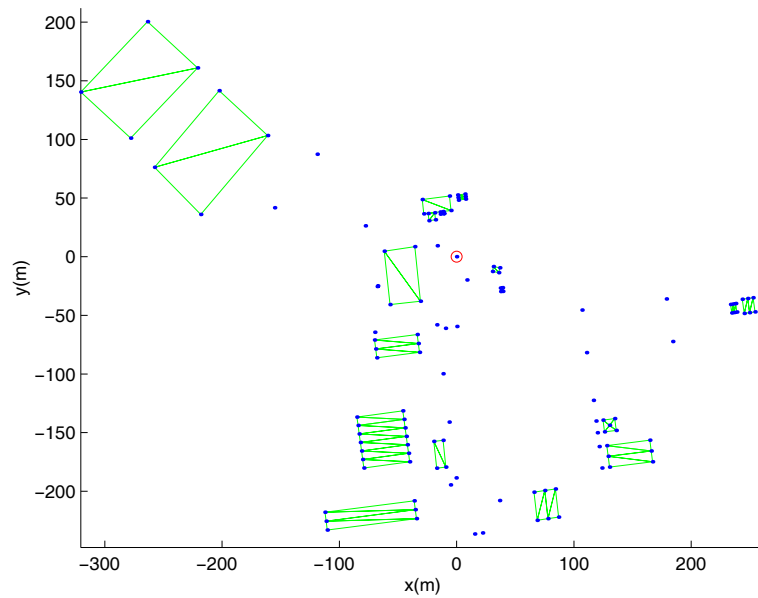


Figure 5.3: *Electronic map of area surrounding the ground station. The surrounding buildings and features are divided into 62 separate triangular surfaces. The  $x,y$  coordinates and height of each are measured with respect to the CGS antenna location*

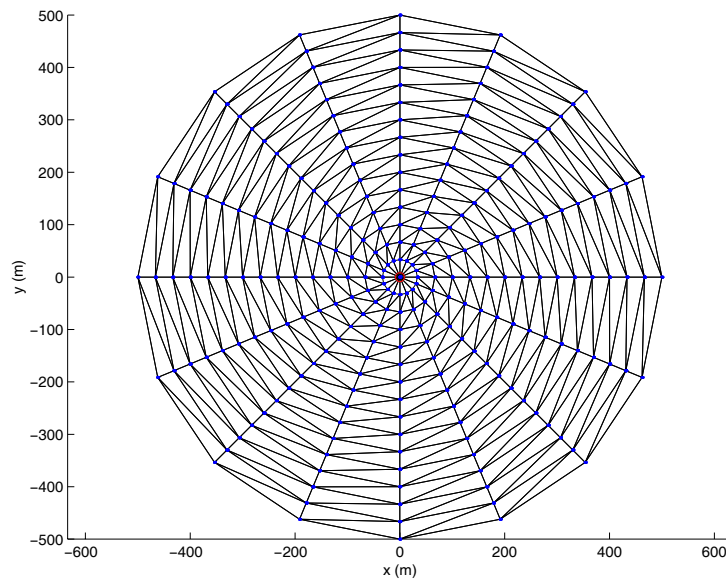


Figure 5.4: *Surrounding terrain divided into 464 individual patches.*

The surrounding terrain is likewise divided into individual triangular patches. The triangular surfaces make up rings of constant distance from the CGS and extend out to cover all of the ground within 500 m from the CGS. For simplification purposes, we assume the terrain to be flat, at a constant elevation height of -2m with respect to the ground station. Note that later, a worst case bistatic cross section is assumed, which tends to account for the approximations made at this step. The resulting 464 triangles are shown in Figure 5.4.

## 5.2 Geometry Analysis

For each triangular surface, we compute the pertinent geometrical information. For a given assumed spacecraft location, the vector representing the incoming signal is  $v_{in}$ , the vector of the specular reflection is  $v_{spec}$ , the vector connecting the surface to the ground station antenna is  $v_{out}$ , and the vector normal to the surface is  $v_n$ , as shown in Figure 5.5.

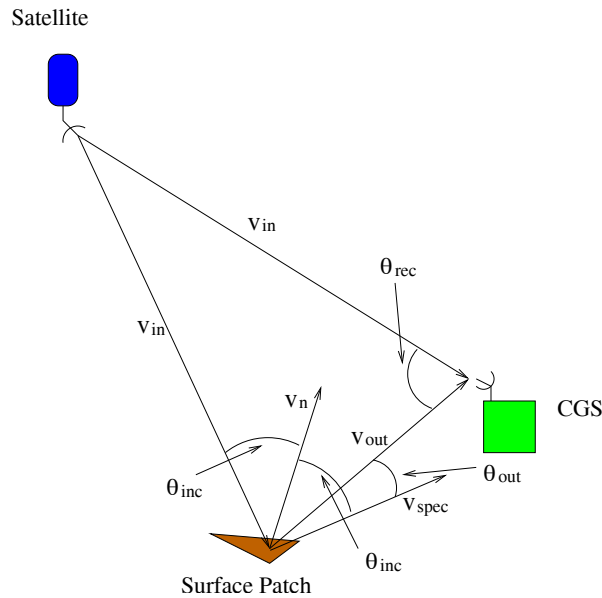


Figure 5.5: *Geometry of an arbitrary surface patch. Because the large distance of the satellite from the CGS, the vector connecting the satellite to the CGS and that connecting the satellite to the surface patch are approximated as equal in length and direction.*

From these vectors, we compute  $\theta_{out}$ ,  $\theta_{rec}$ ,  $R_i$ , and  $A_i$ , where

$\theta_{out}$  = angle between  $v_{spec}$  and  $v_{out}$

$\theta_{rec}$  = angle between  $v_{in}$  and  $v_{out}$

$R_i$  = distance between scatterer and CGS antenna

$A_i$  = area of surface as seen from the satellite.

The resulting geometry calculations from the buildings and the terrain are shown in Figures 5.6 and 5.7, respectively.

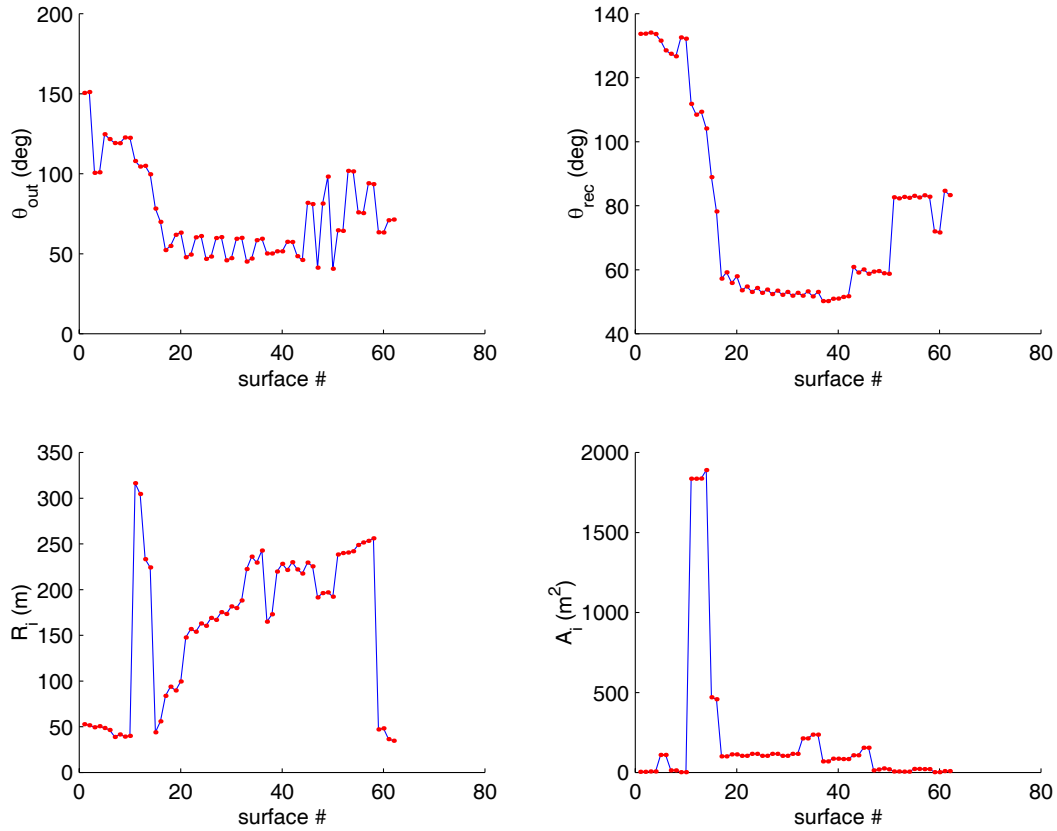


Figure 5.6: *Geometry results for surrounding buildings. The x axis represents the patch number of the surface, which is arbitrarily assigned. For each surface,  $\theta_{out}$  and  $\theta_{rec}$  are never lower than  $45^\circ$*

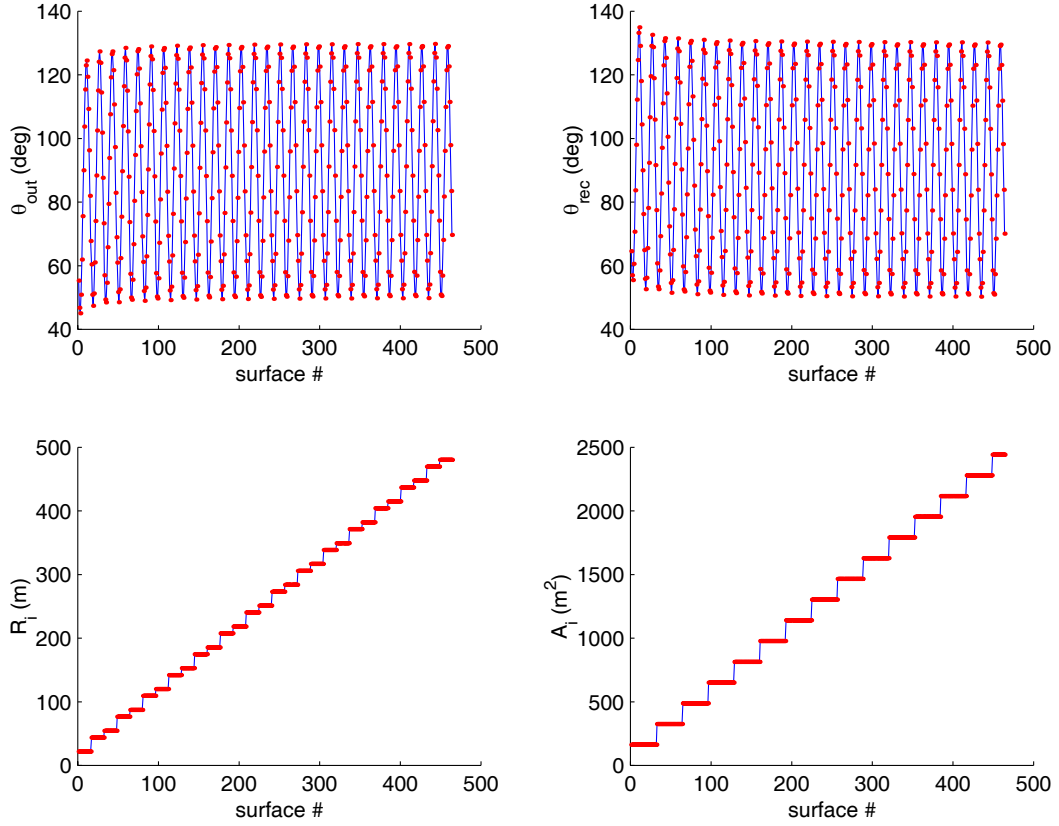


Figure 5.7: *Geometry results for surrounding terrain. The x axis represents the patch number of the surface, which is arbitrarily assigned. The area of the patches increases as the distance from the CGS increases.  $\theta_{out}$  and  $\theta_{rec}$  are never lower than  $45^\circ$ .*

### 5.3 Interference Evaluation

The knowledge of the geometrical parameters of each surface patch allows us to calculate the power of the reradiated satellite signal received by the CGS antenna. The relationship between the transmitted power and the received power of a radar system is defined by the radar equation. One form of the bistatic radar equation sums the contribution from each possible scatterer[3],

$$P_r = \frac{\lambda^2}{(4\pi)^3} \sum_{i=1}^N \frac{P_t G_i^2 \sigma^0(\theta_2 - \theta_1) \Delta A_i}{R_i^4}. \quad (5.1)$$

Equation (5.1) assumes the transmitter and the receiver to be the same instrument. For separate transmitters and receivers,  $G_i^2$  becomes  $G_t G_i$  and  $R_i^4$  becomes  $R_t^2 R_i^2$ . In this particular application,  $P_t$ ,  $G_t$  and  $R_t$  are constant, allowing Equation (5.1) to be rewritten as

$$P_r = \frac{\lambda^2 P_t G_t}{(4\pi)^3 R_t^2} \sum_{i=1}^N \frac{G_i \sigma^0(\theta_{out}) \Delta A_i}{R_i^2}, \quad (5.2)$$

where

- $P_r$  = power received
- $P_t$  = power transmitted
- $G_t$  = gain at transmitting antenna
- $G_i$  = gain at receiving antenna in the direction of the scatterer
- $\lambda$  = wavelength of the transmitted signal
- $R_t$  = distance between satellite and surface patch
- $R_i$  = distance between surface patch and CGS
- $\Delta A_i$  = area of each incremental surface patch
- $\sigma^0(\theta_{out})$  = the nominal bistatic radar cross section of the patch
- $(\theta_{out})$  =  $\theta_2 - \theta_1$ , the angle between the signal reradiated toward the CGS and the specular reflection.

Equation (5.2) represents the power received at the CGS after the signal has reflected off of the surroundings, in this case the multipath, or interference. The power received at the CGS directly (i.e. the desired signal which has not bounced) is defined in [8] by Equation (5.3), and is also known as the link, or beacon, equation,

$$P_r = \frac{P_t G_t \lambda^2 G_r}{(4\pi)^2 R_t^2}, \quad (5.3)$$

where  $G_r$  is the gain at the receiving antenna in the direction of the satellite.

Dividing Equation (5.2) by Equation (5.3), we obtain an interference-to-signal ratio,

$$\frac{P_{r_{indirect}}}{P_{r_{direct}}} = \frac{\sigma^0(\theta_{out})}{4\pi G_r} \sum_{i=1}^N \left( \frac{G_i A_i}{R_i^2} \right). \quad (5.4)$$

In this interference-to-signal ratio,  $A_i$  and  $R_i$  are computed directly by the geometry analysis.  $G_i$  is obtained by computing  $\theta_{rec}$  and looking up its corresponding gain within the CGS antenna pattern, as shown in Figure 5.8.

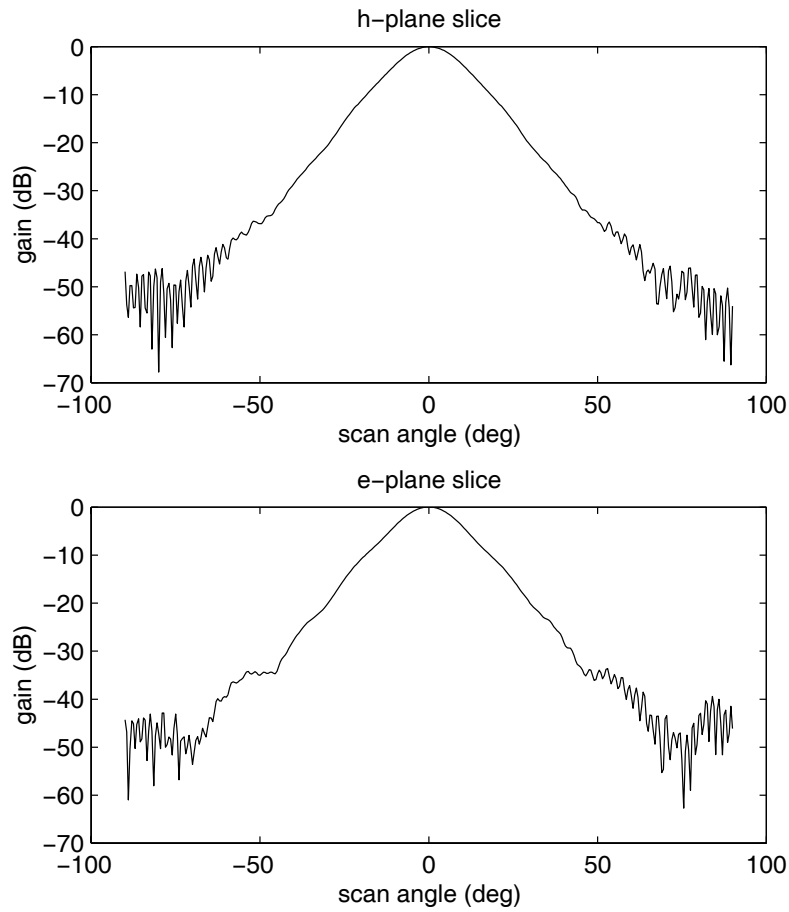


Figure 5.8: *Perpendicular slices through the CGS antenna pattern. The main beam, as is evident in the figure, is very broad. This is according to the CGS design, to minimize the sensitivity of the gain of the received signal when the antenna points at the satellite. (See also Fig. 3.6)*

Since the CGS antenna points directly at the satellite during reception,  $G_r$  is approximated as 1.  $\sigma^0(\theta_{out})$  is a measure of the reflective properties of a scattering surface and is dependent on the geometry of the problem. In particular, it is dependent on the angle between the specular reflection of the transmitted signal and the vector pointing to the receiving antenna. This angle is labelled  $\theta_{out}$  in this analysis and is computed in the geometry analysis.  $\sigma^0(\theta_{out})$  is large if  $\theta_{out}$  is small and it is small if  $\theta_{out}$  is large. This dependence on  $\theta_{out}$  is depicted in Figure 5.9 for scatterometer systems, in which the transmitting and receiving antenna are one and the same.

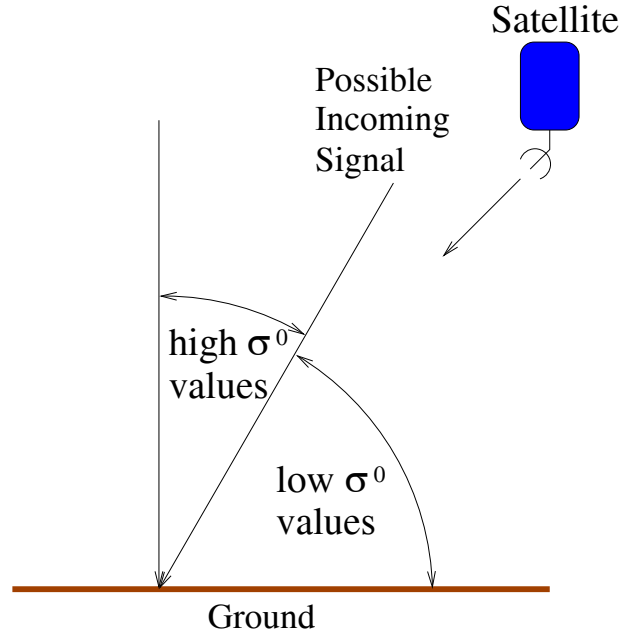


Figure 5.9:  $\sigma^0$  dependence on incidence angle for scatterometers.

In the case of the QuikSCAT CGS, for each surface patch in question,  $\theta_{out}$  is higher than  $45^\circ$ , as seen in Figures 5.7 and 5.6. In light of this result, -10 dB for buildings and -20 dB for terrain are reasonable worst-case estimates for  $\sigma^0(\theta_{out})$ .

## 5.4 Analysis Results and Conclusion

Applying the appropriate parameters and simplifications to Equation (5.4) yields the interference-to-noise ratios shown in Figure 5.10.

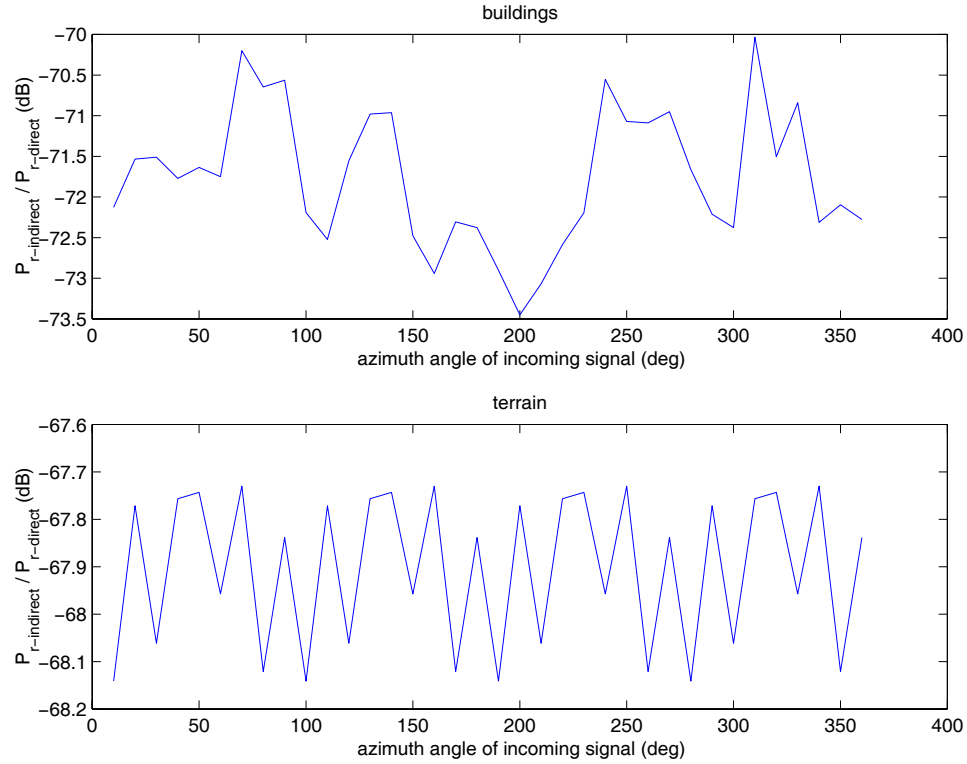


Figure 5.10: *Interference-to-signal ratio as a function of azimuth angle of incoming signal. Depending on the location of the satellite, the azimuth angle of the signal will vary, changing the geometry of the problem. The results, however, show only a minimal dependence on the azimuth angle.*

Figure 5.10 shows that the interference-to-signal ratio of the analyzed multipath is lower than -60 dB for all azimuth angles of the incoming signal. On a linear scale, this means that the interference caused by multipath has less than one millionth the strength of the incoming signal. For the QuikSCAT CGS, this is an acceptable value.

Figure 5.11 shows a graph of the progressive summation of the interference-to-signal ratio. For the buildings, it continues to increase until all scattering surfaces are summed. For the terrain, the contribution becomes less and less with increasing distance from the CGS. It levels off around -68 dB. This justifies the cutoff at 500m used in this analysis.

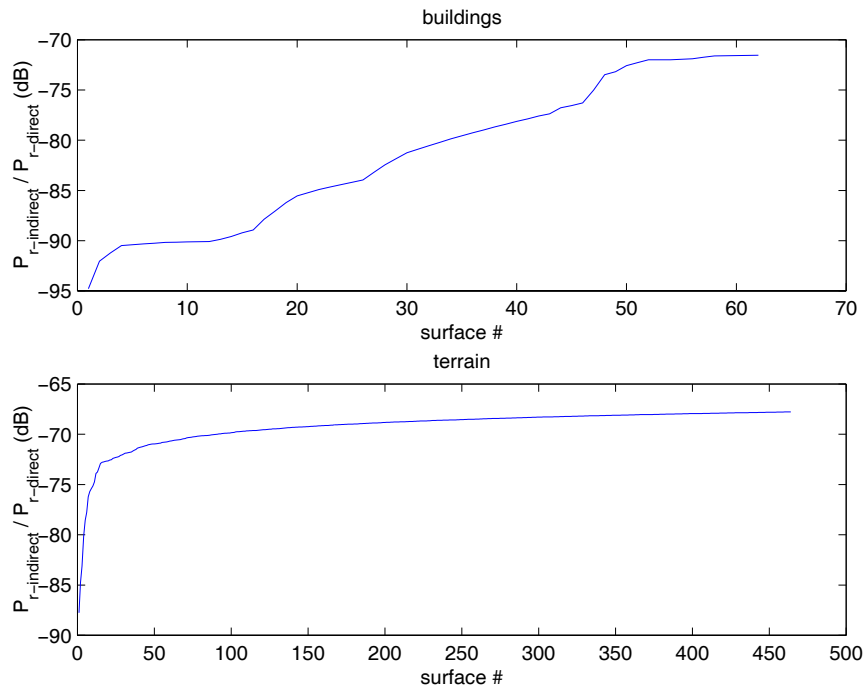


Figure 5.11: *Summation of interference-to-signal ratio. The results level off for the terrain, justifying the 500m cutoff.*

The analysis presented in this chapter shows that multipath of surrounding buildings and terrain causes negligible effects on the received signal at the CGS. This eliminates the need to compensate for its effects in the ground processing of the CGS data.

## Chapter 6

### QuikSCAT CGS Frequency Analysis

Two main independent aspects of the CGS data are analyzed for calibration purposes. One is the power of the signal. The other is the signal frequency. Both are functions of time. The power analysis allows for the verification of the satellite's PRI, attitude, transmitting power, antenna rotation rate and range/Doppler tracking table implementations to within reasonable accuracies. It has also aided in the findings of a 1 sec CGS timing error, a 1 sec GPS satellite timing error [9] and antenna rotation WOW and low speed variation. The frequency analysis enables observation of the instrument local oscillator (LO) and CGS LO offsets and the independent verification of the PRI and the timing errors. This chapter describes the processing of the CGS data in the frequency analysis. It also discusses the implementation of a matched filter, which improves the signal-to-noise ratio of the CGS data. It concludes with some possible uses for the frequency analysis and its matched filter.

#### 6.1 CGS Data

As explained in Chapter 2, QuikSCAT data is captured in 10 second intervals by the CGS as the satellite passes through the ground station's field of view. When QuikSCAT passes across the sky at a high enough angle, it illuminates the ground station 4 times with each pass. Initially, the CGS sees the outer beam as the satellite approaches, then the inner beam as it approaches. Next, it again sees the inner beam, but as the satellite recedes away from the CGS and finally, the outer beam as the satellite recedes. For each time the satellite illuminates the CGS, the CGS captures 10 sec of data. If the angle at which it passes over the horizon is too small, the CGS

receives only the outer beam as QuikSCAT approaches and recedes. The CGS, in that case, captures the signal twice for a period of 20 sec each. It stores the data in consecutive files of 100 ms each, which are obtained via ftp from JPL or directly from the ground station server.

The scatterometer signal is sampled at a rate of 5.1875 MHz, resulting in 518750 samples per raw datafile. The received signal also contains noise and a constant DC offset. These are taken into account in the frequency analysis of the data. Along with the CGS raw data files, BYU also has access to the QuikSCAT L1A data files, which contain all of the measurements of the satellite's position, pointing, attitude, Doppler compensation and other important geometric factors. These are stored in files according to the revolution number of the QuikSCAT mission.

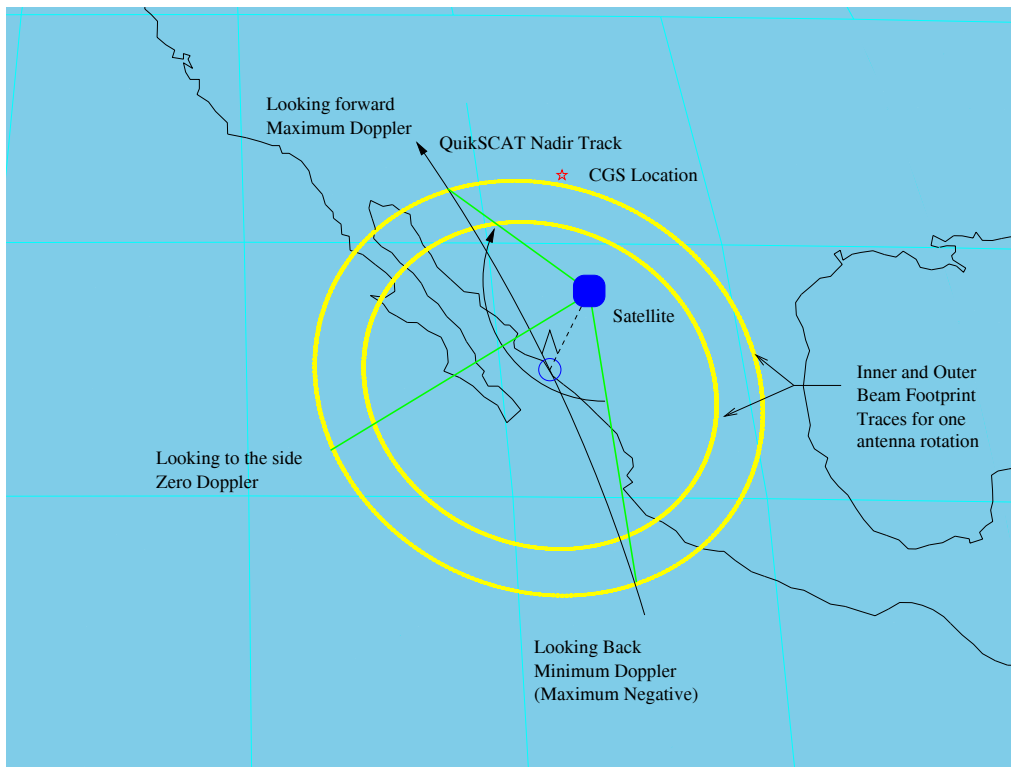


Figure 6.1: *QuikSCAT geometry including backward, side and forward looks. The inner and outer beam footprint traces are shown for a single antenna rotation.*

## 6.2 Expected Frequency Variation

Because the SeaWinds Scatterometer uses a rotating pencil beam antenna, the signal is subjected to a different Doppler shift at different azimuth angles. When looking forward, in the along track direction, the Doppler shift is at its maximum. Looking backward, the Doppler shift is at a minimum. When looking to the side, in the cross track direction, the Doppler shift is zero (see Figure 6.1).

The antenna rotation results in a sinusoidal variation in the Doppler shift. Since this Doppler shift is unwanted in the wind retrieval calculations, SeaWinds includes a varying frequency bias in its transmitted signal, called the Doppler compensation, or commanded Doppler. This sinusoidal frequency bias is equal and opposite to the predicted Doppler frequency and effectively cancels out the Doppler effect, as shown in Figure 6.2.

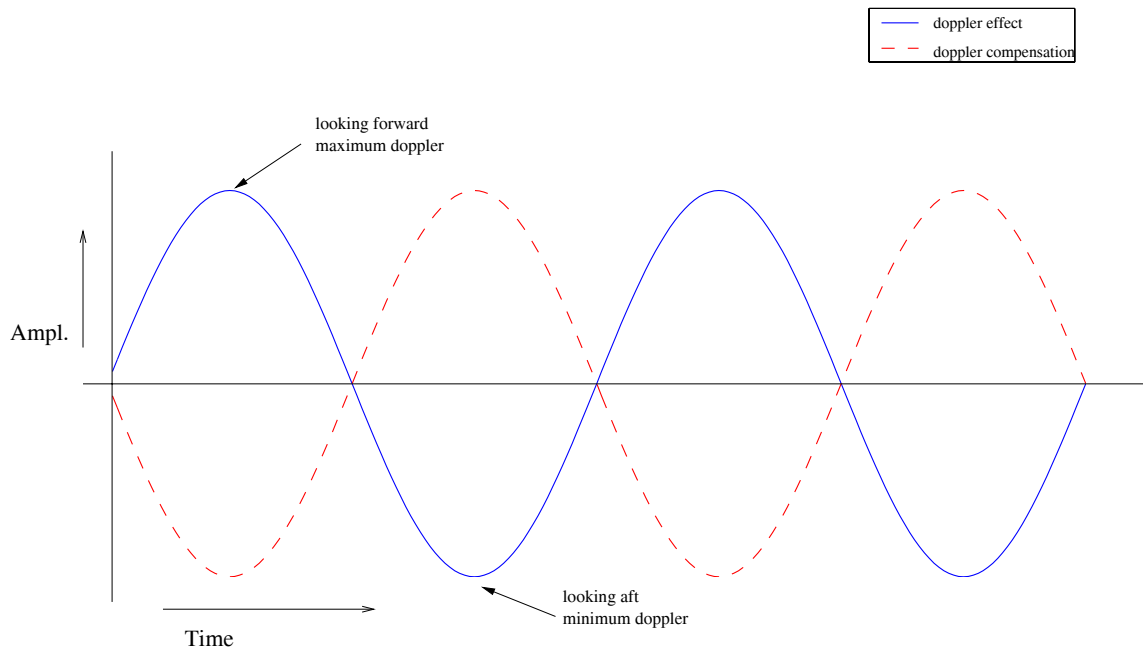


Figure 6.2: *Plot of Doppler effect and Doppler compensation. The Doppler compensation is designed to cancel out the Doppler effect in the CGS data.*

### 6.3 Steps in the Frequency Analysis

This section describes the steps used to compute the frequency of each pulse received by the CGS. The procedure begins by determining the start time of each pulse. Each pulse is then extracted from the data. The frequency spectrum is then computed by means of an FFT. The spectrum is filtered to determine the center frequency of the pulse. The remainder of this section explains these steps in detail and discusses techniques to improve the resolution of the procedure.

The frequency analysis begins by conducting some preliminary processing on one of the raw data files in which the amplitude of the received signal is estimated to be fairly large, i.e. at a time when the main beam of the instrument antenna passes over the CGS. The purpose of this is to find the beginning time of one of the pulses in the data. This is accomplished by extracting a 20 ms window of the data and convolving it with a 1.5 ms square wave. The output of the convolved portion of the data is a series of triangle waves, the peaks of which indicate the trailing edges of the pulses. The maximum of the convolved data then indicates the trailing edge of a desired pulse which represents a known point in time from which the start times of all other pulses in the data can be deduced (see Figure 6.3).

Knowing the start times of the pulses, the next step in the frequency analysis is to process the data in 200 ms segments (2 consecutive raw data files) at a time. From each of these 200 ms segments, 18 consecutive pulses are extracted, each with a buffer on either side to assure that the pulse is not cut off at a boundary. The number 18 was selected so as to extract all of the complete pulses within the 200 ms window of data.

To find the center frequency of each pulse, the FFT of the pulse is computed. Then the FFT is filtered by convolving it with a 375 MHz (the bandwidth of the chirp) wide square wave. This produces a triangle wave, the center or maximum of which indicates the upper edge of the frequency spectrum of the chirp i.e. the pulse. Figure 6.4 shows examples of raw pulse data, the FFT of a pulse and the filtered FFT of a pulse.

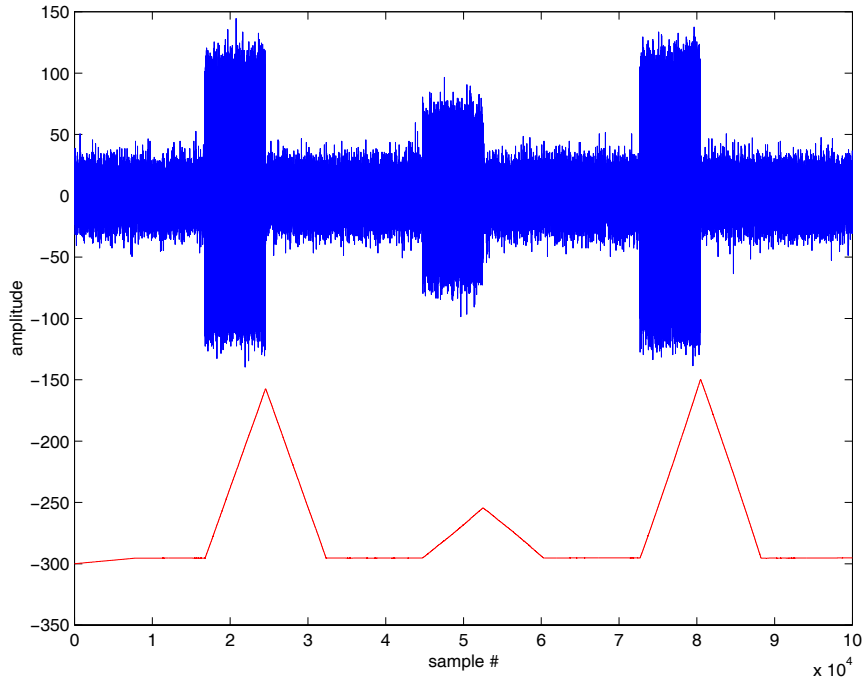


Figure 6.3: *20 ms window of CGS data. Envelope filtered data is shown below. Peaks in the filtered data indicate trailing edges of pulses*

As explained in Section 6.2, the received frequency varies sinusoidally, according to the Doppler compensation. Because of the limited time in which the scatterometer points directly at the CGS, the data received above the noise floor is sparse and occurs only in certain intervals of time. The sinusoidal frequency variation therefore only appears in discrete clusters, as shown in Figure 6.5. The top graph in Figure 6.5 shows the received frequency versus time with a sinusoid fit through the data points. The bottom graph shows the difference between the actual received frequency and the expected frequency. The difference, or frequency error, lies within a band approximately 10 kHz wide.

Potential applications of the frequency analysis require more precise knowledge of the received frequency. It is therefore desirable to improve the resolution of the frequency and decrease the width of the error band. When analyzing simulated data with a high signal-to-noise ratio (SNR), the highest resolution obtainable is 600 Hz,

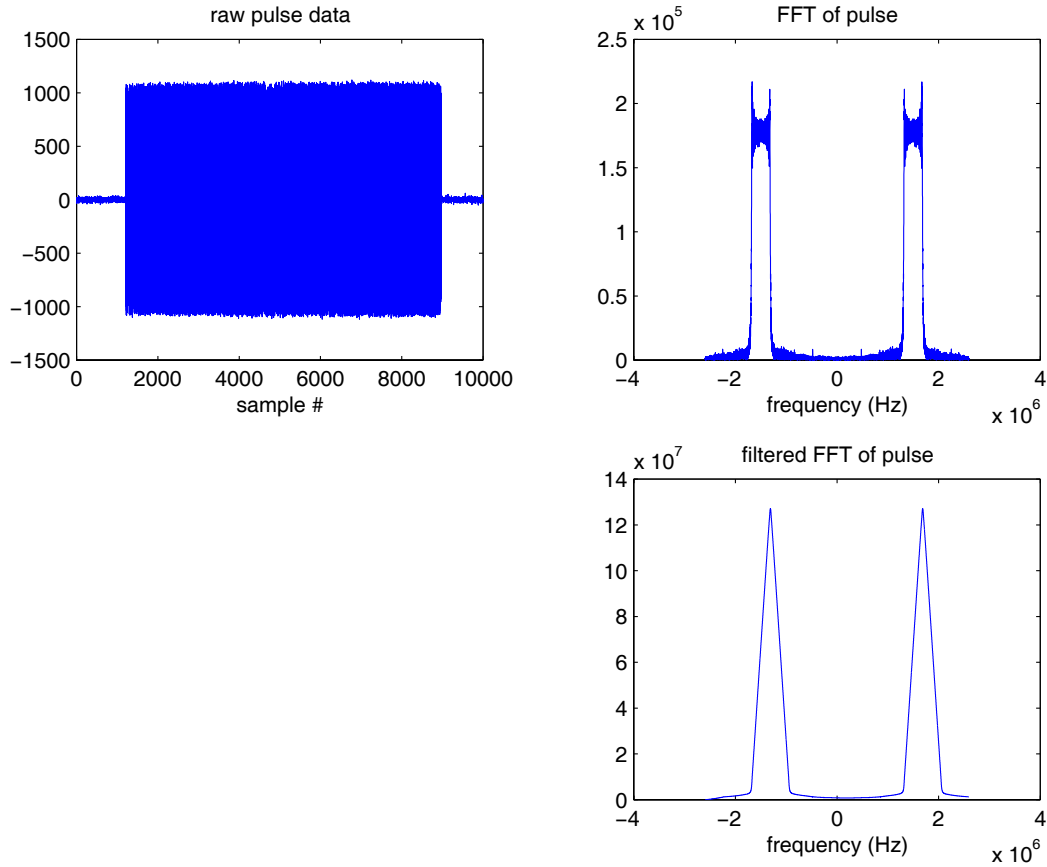


Figure 6.4: *Analysis of a typical received pulse. The upper left figure shows raw pulse data over a 2 ms period. The upper right figure shows the FFT of the extracted pulse. The lower right figure shows the filtered FFT of the pulse. The peaks of the triangles indicate the right edges of the pulse frequency spectrum.*

resulting from the 1.5 ms pulse. Three different resolution enhancement techniques were explored, in the attempt to decrease the frequency error width.

The first technique is to zero-pad the extracted pulses. This artificially lengthens the duration of the data segment. It thereby increases the time bandwidth product, which dictates the resolution. The second improvement technique is that of interpolating the filtered spectrum of the pulse around the peak. This adds more data points to the critical area and uses a cubic spline routine to estimate their amplitude. The third technique investigated uses the sides of the triangle created by the

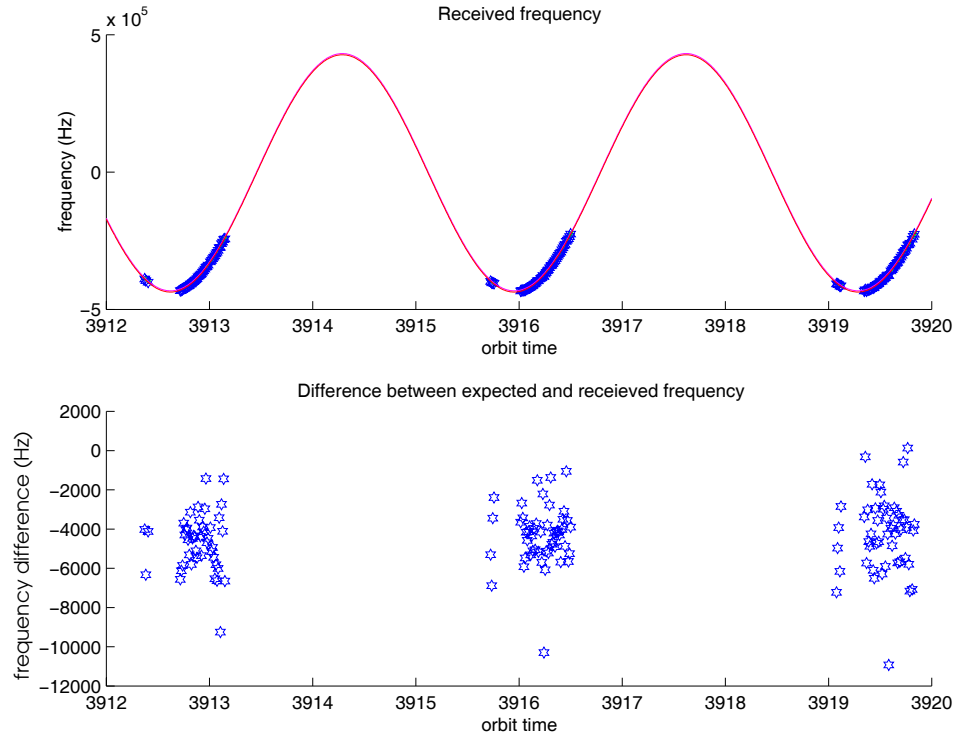


Figure 6.5: *Sample results of the initial frequency analysis. The top plot shows the received frequency of the satellite signal with the carrier removed. Each point represents a pulse whose amplitude is a detectable amount above the noise floor. The continuous curve is a sinusoid fit to the data. The bottom plot shows the difference between the frequency of the received data and the calculated expected received frequency. The difference lies within an error band approximately 10 kHz wide.*

filtered spectrum to estimate the location of the peak. This is similar to the interpolation technique in that it uses calculated points to estimate further points. Instead of just using just six points near the peak, however, it uses hundreds of points along the sides to estimate the peak. Lines are fit through the sides of the triangle and extended beyond the peak. The intersection of the two lines indicates the location of the peak. Examples of the frequency resolution enhancement methods are shown in Figure 6.6.

The three resolution enhancement techniques have been evaluated by analyzing their results on simulated data. Figure 6.7 compares their results for one simulated 10 s capture. Each of the resolution enhancement techniques reduce the width of the

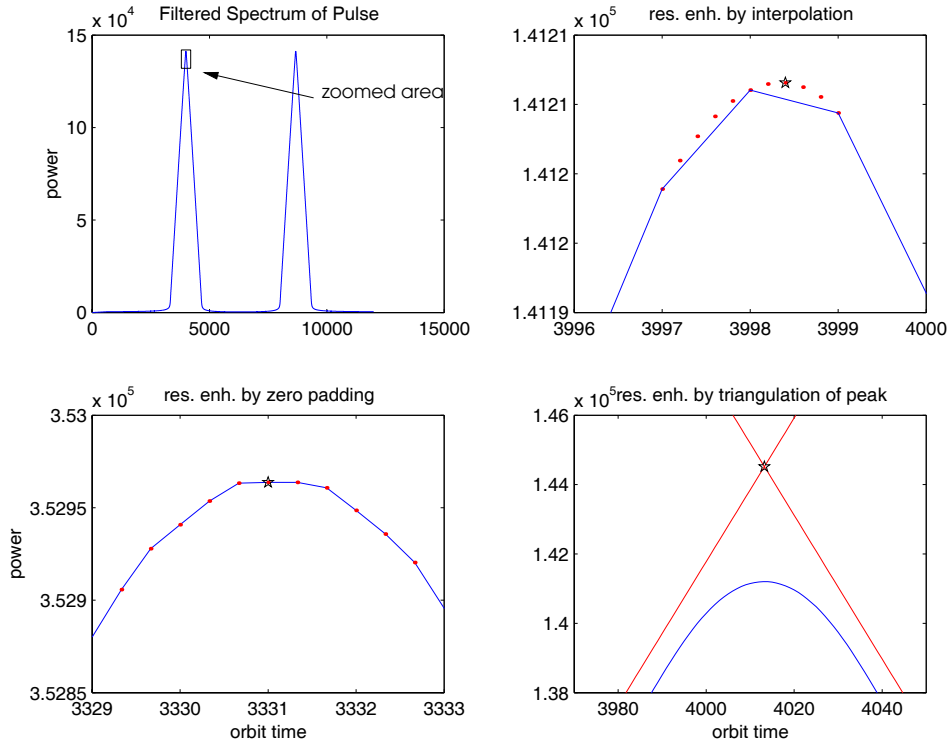


Figure 6.6: *Frequency enhancement techniques. The upper left plot shows the filtered FFT of a pulse (see Figure 6.5). The upper right plot shows the peak of the triangle at normal resolution with points added by interpolation. The peak location is determined from the added points. The lower left plot shows the peak of the triangle at a higher resolution, enhanced by zero padding the pulse data. The resolution enhancement factor for the given plot is 3. The lower right plot shows the peak of the triangle as well as lines which are fit to the sides of the triangle and extend past the peak. The intersection of the lines indicates the location of the peak of the triangle. The stars show the estimated locations of the peak.*

error band by a factor of approximately 2. Despite using target resolution enhancement factors of 3 or more for the interpolation and zero padding techniques (i.e. interpolating to points with one third of the original spacing, or zero padding twice the length of the pulse so as to artificially triple its length), the limit to the reduction of the error band width remains at a factor of 2. This limit is most probably due to residual noise in the data simulation and the frequency determination.

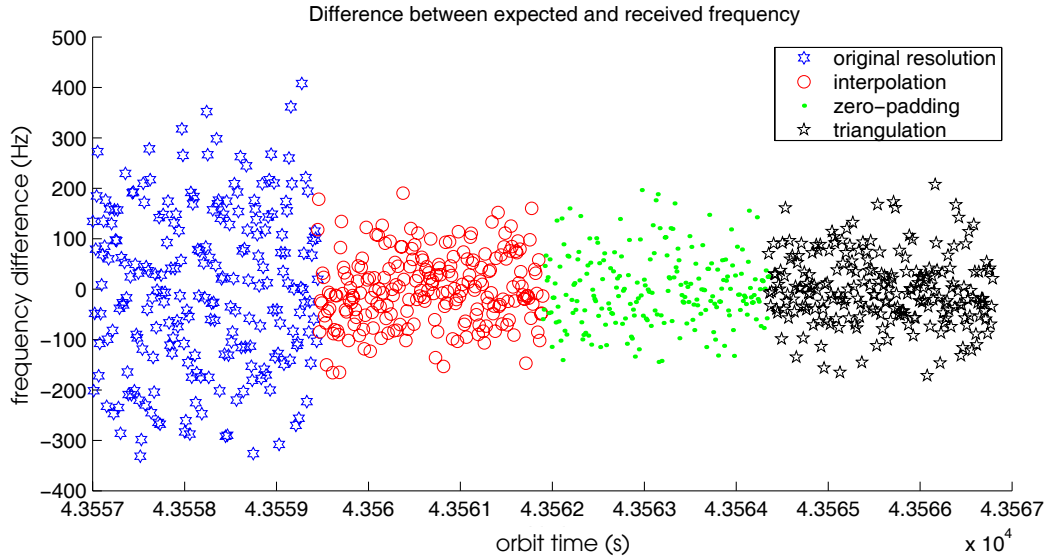


Figure 6.7: *Resolution enhancement results for simulated data. The plot represents the difference between the expected frequency and the actual received frequency. The simulated data set is split up into four portions, each 2.5 s long. The first segment is simulated using the original resolution. The interpolation technique is used to analyze the second segment. The zero padding technique is used to analyze the third segment. The triangulation method is used to analyze the last segment. Each of the resolution enhancement techniques decreases the width of the error band by a factor of 2 from the original.*

In spite of the improvement in the frequency resolution, the resolution enhancement techniques do not significantly decrease the width of the error band in the actual data. The error band width depends also on the SNR of the received signal. Lower SNR causes greater errors. Therefore, the next step of the frequency analysis is to increase the SNR with the aid of a matched filter, as explained in Chapter 7.



## Chapter 7

### Matched Filter Implementation

In order to reduce the error in the estimate of the received frequency, the frequency analysis increases the SNR of the received signal by means of the matched filter, also known as the optimal filter. As described by [8], given the assumption of a flat noise spectrum, the spectrum of the optimal filter,  $H_{opt}(\omega)$ , for a given signal,  $s_i(t)$ , with the spectrum  $S_i(\omega)$  is defined in Eq. (7.1),

$$H_{opt}(\omega) = K' S_i^*(\omega) e^{-j\omega t_0}, \quad (7.1)$$

where  $K'$  is an arbitrary scale factor. The corresponding time domain signal,  $h_{opt}(t)$  is defined as

$$h_{opt}(t) = K' s_i(t_0 - t). \quad (7.2)$$

The optimal filter, which yields the greatest improvement in SNR, is thus a reverse copy of the input received signal, shifted in time by  $t_0$ . In order to create a copy of a received chirped pulse, it is necessary to know the apparent carrier frequency and the chirp rate. The scatterometer signal is transmitted on a 13.402 GHz carrier. The frequency of the received signal follows the plan shown in Figure 7.1 in the ground station processing.

Because of the undersampling of the 35 MHz signal, the frequency folds over seven times and the resulting signal has an apparent carrier frequency of -1.3125 MHz. The received signal as seen in the CGS data thus follows the following equation:

$$x(t) = \cos \left( (\omega_0 + \omega_d)t + \frac{\alpha t^2}{2} \right), \quad (7.3)$$

where

- $t$  = time
- $\omega_0$  = the effective carrier frequency, -1.3125 MHz
- $\omega_d$  = the commanded Doppler frequency, and
- $\alpha$  = the chirprate, 250.73 MHz/sec.

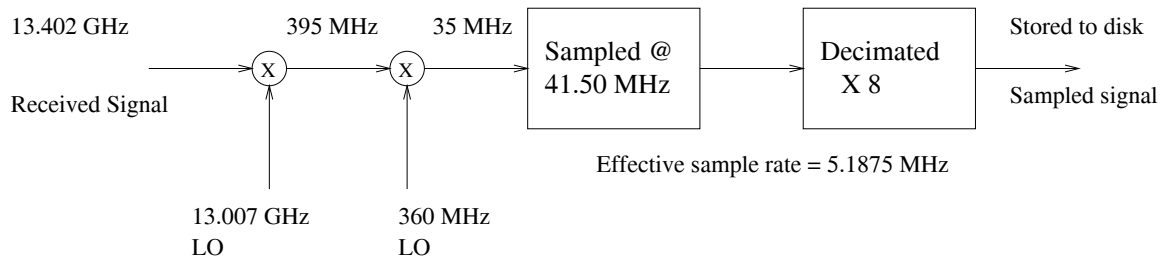


Figure 7.1: *Frequency plan of the CGS. The incoming 13.402 GHz signal is mixed down to 35 MHz and sampled at an effective rate of 5.1875 MHz. The resulting signal is stored to disk.*

In coherent matched filtering, the phase of the signal replica is crucial to the success of the matched filter. Non-coherent processing can also be used. The CGS frequency analysis removes phase issues by using non-coherent matched filtering. This technique replicates the input signal on to two orthogonal bases, one sine and one cosine. Both of these copies are inverted and shifted in time and the input signal is filtered through both. The outputs are then squared and added to remove dependence on the phase of the received signal. A block diagram of the matched filter processing of the CGS frequency analysis is shown in Figure 7.2. The squaring function rectifies the signal and the low pass filter removes any unwanted high frequency harmonics caused by the initial filter,  $h_{opt}(t)$  and by the squaring operation.

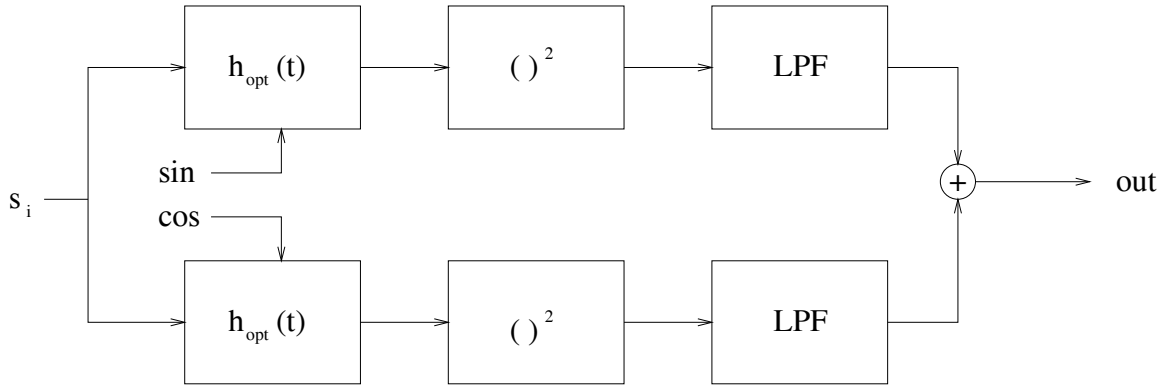


Figure 7.2: Block diagram of matched filtering system. The input signal is convolved with two matched filters, offset in phase by  $90^\circ$ , then squared and low pass filtered. The two filtered signals are then added to produce the output.

## 7.1 Filter Bank

In order to determine the frequency of the received signal, the analysis filters it through a bank of filters, varying the frequency with each consecutive filter. Plotting the total power resulting from each filter yields a curve similar to the one shown in Figure 7.3. The peak of the curve indicates the filter yielding the highest return and therefore representing the closest approximation to the true matched filter. Its frequency then is the closest determination of the frequency of the received pulse.

Preparing the bank of filters requires the choice of a frequency range, in which the true frequency is likely to be found. This frequency range is chosen as a 6 KHz range, centered around an initial estimate. The estimate stems from the FFT of the pulse, previously processed in the CGS frequency analysis.

A typical result from a CGS capture processed with the matched filter is shown in Figure 7.4. The difference between the expected frequencies and the received frequencies of the pulses remain within an error band approximately 2 kHz wide. This is a significant improvement over the initial FFT processing, which yields an error band approximately 10 kHz wide.

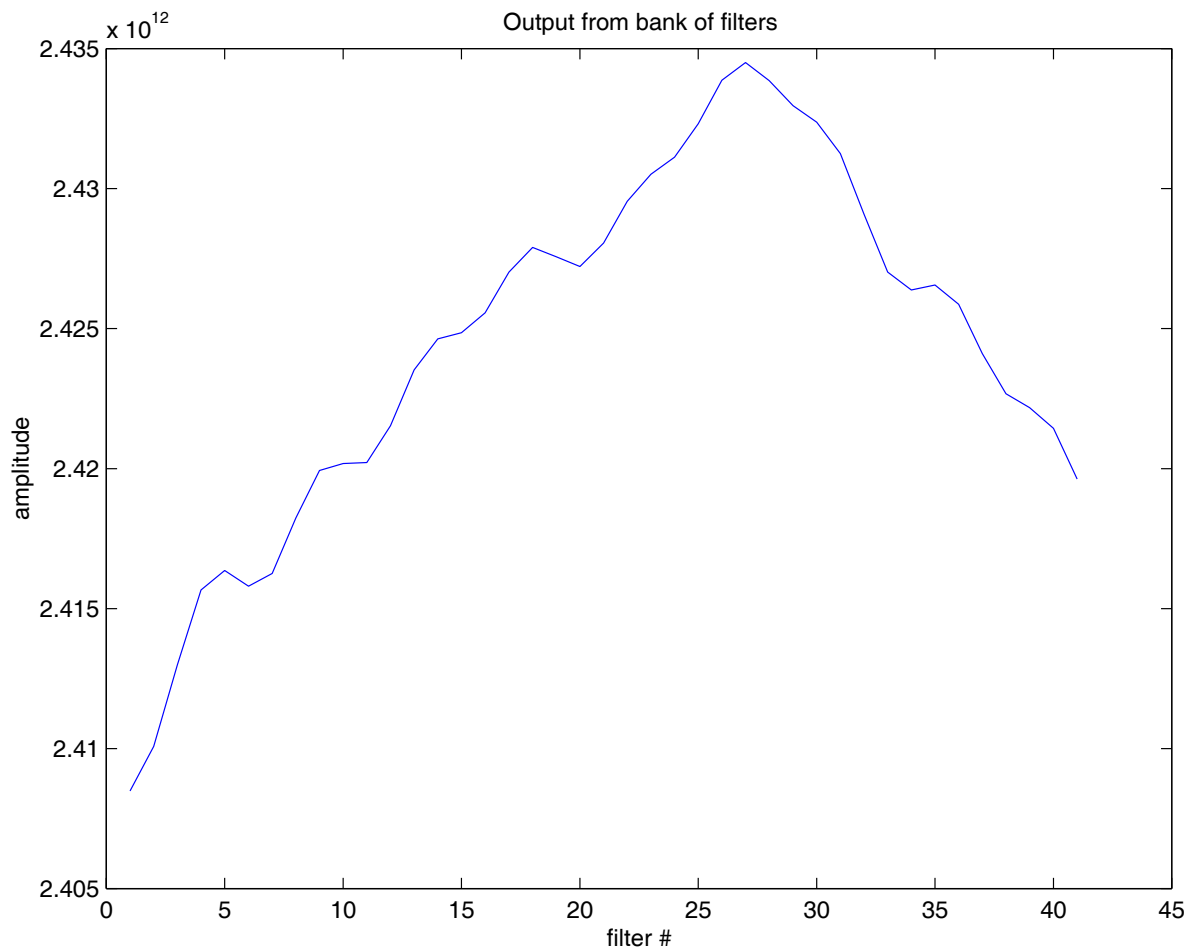


Figure 7.3: *Sample results from the filter bank. The bank of filters consists of 41 different filters, each matched to a different center frequency. The peak of the curve indicates the filter whose frequency is best matched to the received pulse.*

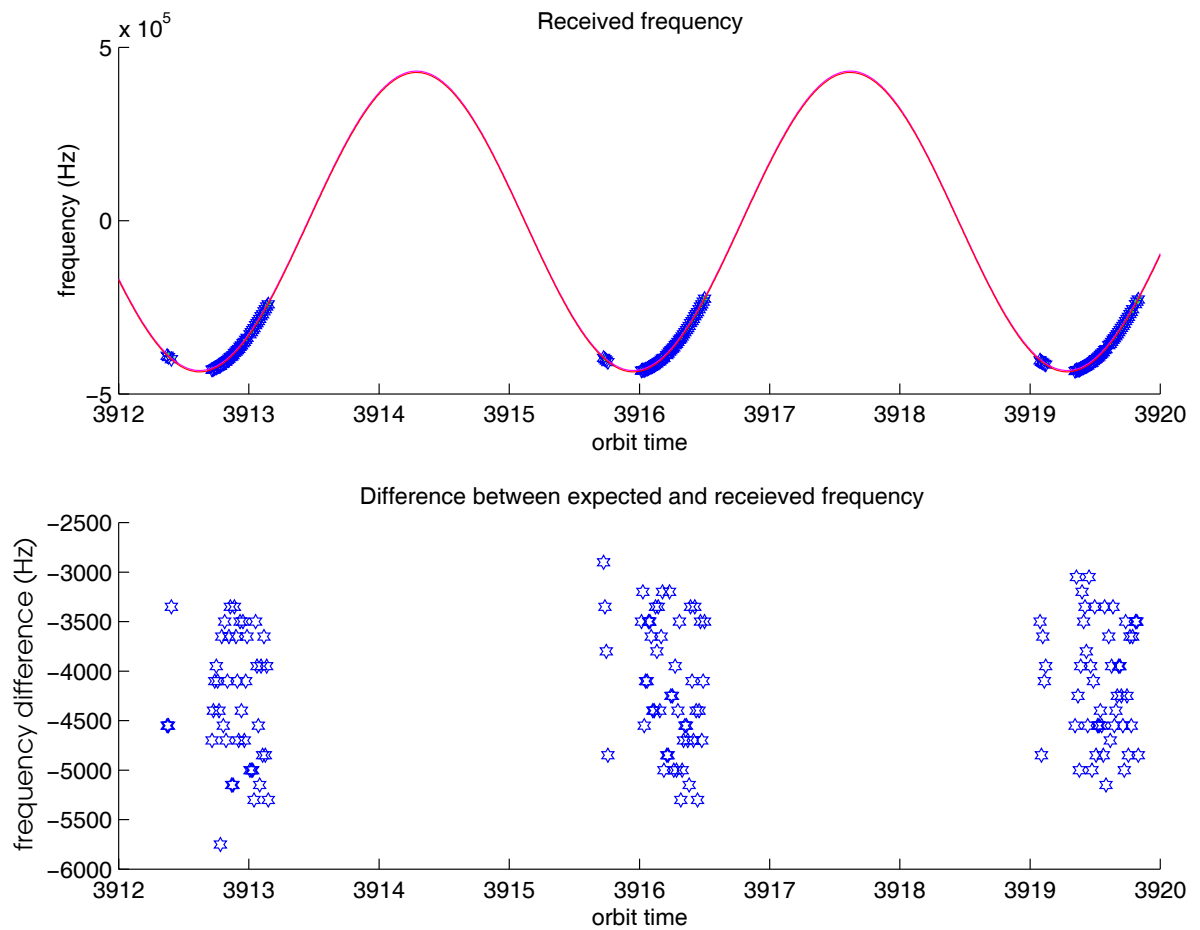


Figure 7.4: *Sample results from matched filter processing. Top plot shows the frequency of received pulses with an amplitude greater than a set threshold. A sinusoid is fit to the data. The bottom plot shows the difference between the calculated expected frequency and the actual received frequency. Compare with Fig. 6.5. Matched filtering decreases the error band from 10 kHz to 2 kHz.*

Consecutive pulses with high SNR, but differing in error by up to 1 kHz, suggest the possibility of oscillator noise. In this case, the error band may be in part due to actual jumps in the transmitted frequency. A more likely cause is the noise in the frequency determination method.

## 7.2 Benefits of the Matched Filter

The main advantage that the matched filter provides is an increase in signal-to-noise ratio. One way to exploit this capability is to use it in the power analysis of the CGS data. Lowering the noise level increases the accuracy of the power determination and allows for reliable measurements beyond the main beam of the antenna pattern.

A lower noise level also makes it possible to determine the power of the SeaWinds signal as received by the CGS at times when the SeaWinds antenna is not pointed directly at the ground station. This offers information about the SeaWinds antenna pattern far beyond the main beam. It enables a partial reconstruction of the antenna pattern over a broad range of angles as shown in Figure 7.5. A longer data capture, over 60 seconds perhaps, would allow for a more complete reconstruction of the antenna pattern. A reconstructed antenna pattern could help in validating the geometry routines used in the CGS data processing. It could also be used to validate the spatial response function of the SeaWinds footprint used in the SeaWinds data processing.

## 7.3 Conclusion

The matched filter is able to decrease the frequency error variance by a factor of approximately five. Despite the improvement in the variance, however, the frequency analysis still cannot provide the accuracy needed for many calibration applications. One of the original motivations for the frequency analysis, for instance, was the determination of the satellite timing. Existing algorithms for timing determination require the knowledge of the frequency to a 1 Hz precision. The frequency analysis can, however, be used to monitor the mean frequency drift of the SeaWinds signal with accuracy.

### outer beam antenna pattern reconstruction

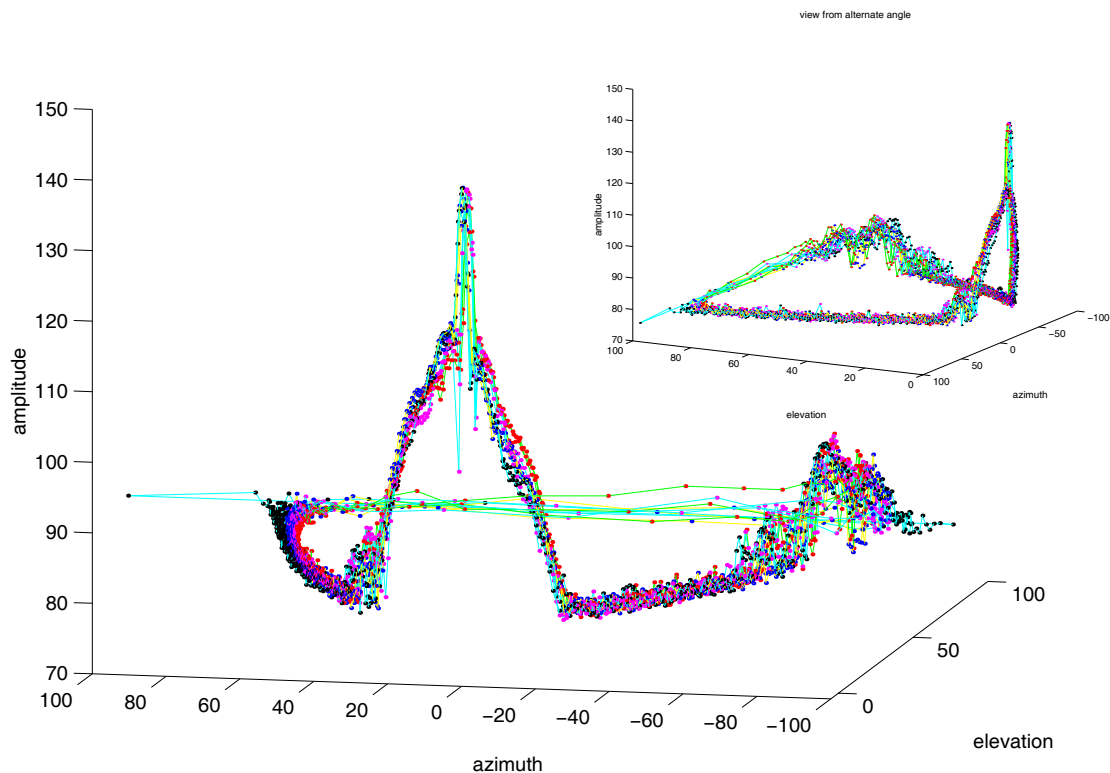


Figure 7.5: *Reconstructed SeaWinds antenna pattern. A portion of the SeaWinds antenna pattern over a range of  $90^\circ$  in elevation and  $\pm 90^\circ$  in azimuth is reconstructed using CGS data. The data reveals a prominent sidelobe at  $-70^\circ$  azimuth and  $60^\circ$  elevation.*

The matched filter, with its SNR improving abilities, also has some additional uses in the CGS calibration efforts. It can be used to enhance the power analysis by effectively lowering the noise. It can also be used to extract the power from the received signal over a wide range of antenna pattern angles. Using the extracted power, a significant portion of the SeaWinds antenna pattern can be reconstructed. The reconstructed antenna pattern can then feasibly be used in the power analysis or in wind retrieval.



## Chapter 8

### Conclusion

This thesis presents key analyses that evaluate the effectiveness and usage of the QuikSCAT Calibration Ground Station. In a general sense, we conclude that the CGS is a tool capable of accurately receiving the signal of the SeaWinds scatterometer. The signal received by the CGS is sensitive enough to perturbations in the spacecraft position, attitude and timing to observe distinct changes in the data caused by the perturbations.

The frequency of the received signal can be determined, but its accuracy is limited. The accuracy is improved using a matched filter, which increases the signal-to-noise ratio (SNR). This chapter points out the contributions of this thesis and lists some areas of possible future research.

#### 8.1 Summary of Contributions

This thesis describes a geometry analysis which provides a method to calculate the Doppler frequency and important antenna pattern angles from SeaWinds telemetry data.

The sensitivity analysis in this thesis determines that the CGS data is sensitive to position, attitude and timing perturbations of the QuikSCAT satellite. However, the mere difference in power between the expected and actual received SeaWinds signal is an unreliable measure to determine spacecraft perturbations. Instead, antenna pattern angle displacement should be used.

The multipath analysis in this thesis evaluates the possible threat of multipath interference in the CGS data. It concludes that the strength of any multipath

interference is better than 60 dB lower than the strength of the directly received signal. This eliminates the need to compensate for multipath interference in CGS data processing.

This thesis describes a method to determine the frequency of the signal received at the CGS. Using a matched filter, the center frequency of the pulses transmitted by SeaWinds can be determined to within  $\pm 1$  kHz. The matched filter increases the SNR of the received signal and provides the ability to reconstruct the SeaWinds antenna pattern over a broad range of angles. The antenna pattern reconstruction reveals a prominent sidelobe in the SeaWinds antenna pattern approximately  $70^\circ$  from boresight.

## 8.2 Future Research

The results from this thesis suggest a number of areas of future research. The perturbation signatures presented in the sensitivity analysis can be enhanced. With refinement they could aid in determining spacecraft perturbations and provide an independent verification of current perturbation determination techniques.

The multipath analysis can be extended to include the interference caused by the CGS roof. One way to accomplish this might be to use the Method of Moments technique to compute the currents along the corrugations of the roof caused by the incoming SeaWinds signal. The computed currents could be used to determine the electric field strength in the far field, which could then be compared to the strength of the directly received SeaWinds signal. The multipath effect from the CGS roof can also be approximated by the same method presented in this thesis for the buildings and surrounding terrain. A preliminary analysis using this method showed the interference to signal ratio to be approximately -60 dB for multipath off of the CGS roof. This result is consistent with the results from the buildings and surrounding terrain, in that the multipath effect is small enough to neglect and does not require compensation.

The matched filter can be used in the power analysis to increase the SNR. This could improve the accuracy in determining and exploiting the power of the CGS data.

The antenna pattern reconstruction can also be extended to include a greater range of antenna pattern angles. Extracting the power of the non-intended beam, i.e. the power of the outer beam during an inner beam capture, is one way to include a greater set of angles. Another option is to look at data over a twenty second capture or longer, if the CGS is prepared for such a data capture.

Another type of antenna pattern reconstruction might be performed. Using the geometry analysis and the SeaWinds telemetry data, coupled with CGS data, the antenna pattern could be reconstructed on the ground. The boresight location of this reconstructed antenna pattern could be compared with the boresight location from the telemetry data to calibrate the timing or attitude of the QuikSCAT satellite.



## Bibliography

- [1] David. G. Long, “Land and ice applications of SeaWinds data,” in *Proceedings of the International Geoscience and Remote Sensing Symposium*, Vol. 3, pp. 1220–1222, Hilton Hawaiian Village, Honolulu, Hawaii, July 24-28 2000.
- [2] Ivan S. Ashcraft, David G. Long, Arden T. Anderson, Steven L. Richards, Michael W. Spencer, and Brian Jones, “Sigma-0 retrieval from SeaWinds on QuikSCAT,” in *Earth Observing Systems, IV*, William L. Barnes, Editor, Proceedings of SPIE, Vol. 4, pp. 171–178, July 1999.
- [3] Fawwaz T. Ulaby, Richard K. Moore, and Adrian K. Fung, *Microwave Remote Sensing*, Vol. 2, Artech House Inc., Norwood, MA, 1981.
- [4] David. G. Long and Michael W. Spencer, “Radar backscatter measurement accuracy for a spaceborne pencil-beam wind scatterometer with transmit modulation,” *IEEE Transactions on Geoscience and Remote Sensing*, Vol. 35, No. 1, pp. 102–114, January 1997.
- [5] Michael W. Spencer, Chialin Wu, and David G. Long, “Tradeoffs in the design of a spaceborne scanning pencil-beam scatterometer,” *IEEE Transactions on Geoscience and Remote Sensing*, Vol. 35, No. 1, pp. 115–126, January 1997.
- [6] Michael W. Spencer, Chialin Wu, and David G. Long, “Improved resolution backscatter measurements with the SeaWinds pencil-beam scatterometer,” *IEEE Transactions on Geoscience and Remote Sensing*, Vol. 38, No. 1, pp. 89–104, 2000.
- [7] David G. Long, Peter K. Yoho, Arden T. Anderson, Jon Adams, James P. Lux, and Frank Cheng, “Quikscat calibration results using the calibration ground

station,” Prepared for the SeaWinds Science Working Team Meeting at JPL, Pasadena, California, November 3 to 5, 1999.

- [8] Harold R. Raemer, *Radar Systems Principles*, CRC Press, Inc., 1997.
- [9] Peter K. Yoho, Arden T. Anderson, David G. Long, Jon Adams, James P. Lux, and Frank Cheng, “SeaWinds on QuikSCAT calibration using a calibration ground station,” in *Proceedings of the International Geoscience and Remote Sensing Symposium*, Vol. 3, pp. 1039–1041, Hilton Hawaiian Village, Honolulu, Hawaii, July 24-28 2000.